

Utah State University

DigitalCommons@USU

All Graduate Theses and Dissertations

Graduate Studies

5-2015

High Regression Rate Hybrid Rocket Fuel Grains with Helical Port Structures

Sean D. Walker
Utah State University

Follow this and additional works at: <https://digitalcommons.usu.edu/etd>

 Part of the [Aerospace Engineering Commons](#)

Recommended Citation

Walker, Sean D., "High Regression Rate Hybrid Rocket Fuel Grains with Helical Port Structures" (2015). *All Graduate Theses and Dissertations*. 4618.
<https://digitalcommons.usu.edu/etd/4618>

This Thesis is brought to you for free and open access by the Graduate Studies at DigitalCommons@USU. It has been accepted for inclusion in All Graduate Theses and Dissertations by an authorized administrator of DigitalCommons@USU. For more information, please contact digitalcommons@usu.edu.



HIGH REGRESSION RATE HYBRID ROCKET FUEL GRAINS WITH
HELICAL PORT STRUCTURES

by

Sean D. Walker

A thesis submitted in partial fulfillment
of the requirements for the degree

of

MASTER OF SCIENCE

in

Aerospace Engineering

Approved:

Dr. Stephen A. Whitmore
Major Professor

Dr. David Geller
Committee Member

Dr. R. Rees Fullmer
Committee Member

Dr. Mark R. McLellan
Vice President for Research and
Dean of the School of Graduate Studies

UTAH STATE UNIVERSITY
Logan, Utah

2015

Copyright © Sean D. Walker 2015

All Rights Reserved

Abstract

High Regression Rate Hybrid Rocket Fuel Grains with Helical Port Structures

by

Sean D. Walker, Master of Science

Utah State University, 2015

Major Professor: Dr. Stephen A. Whitmore
Department: Mechanical and Aerospace Engineering

Hybrid rockets are popular in the aerospace industry due to their storage safety, simplicity, and controllability during rocket motor burn. However, they produce fuel regression rates typically 25% lower than solid fuel motors of the same thrust level. These lowered regression rates produce unacceptably high oxidizer-to-fuel (O/F) ratios that produce a potential for motor instability, nozzle erosion, and reduced motor duty cycles. To achieve O/F ratios that produce acceptable combustion characteristics, traditional cylindrical fuel ports are fabricated with very long length-to-diameter ratios to increase the total burning area. These high aspect ratios produce further reduced fuel regression rate and thrust levels, poor volumetric efficiency, and a potential for lateral structural loading issues during high thrust burns. In place of traditional cylindrical fuel ports, it is proposed that by researching the effects of centrifugal flow patterns introduced by embedded helical fuel port structures, a significant increase in fuel regression rates can be observed. The benefits of increasing volumetric efficiencies by lengthening the internal flow path will also be observed. The mechanisms of this increased fuel regression rate are driven by enhancing surface skin friction and reducing the effect of boundary layer “blowing” to enhance convective heat transfer to the fuel surface. Preliminary results using additive manufacturing to fabricate hybrid rocket fuel grains from acrylonitrile-butadiene-styrene (ABS) with embedded helical

fuel port structures have been obtained, with burn-rate amplifications up to 3.0x than that of cylindrical fuel ports.

(60 pages)

Public Abstract

High Regression Rate Hybrid Rocket Fuel Grains with Helical Port Structures

by

Sean D. Walker, Master of Science

Utah State University, 2015

Major Professor: Dr. Stephen A. Whitmore
Department: Mechanical and Aerospace Engineering

Hybrid rockets are popular in the aerospace industry due to their storage safety, simplicity, and controllability during rocket motor burns. These types of motors use an oxidizer, which is pumped into a pressure vessel containing the solid rocket fuel. However, the fuel used in these motors burn at a much lower rate than traditional solid rocket motors, which have the oxidizer pre-mixed into the fuel. To compensate for this, more oxidizer is pumped into the hybrid rocket motor to increase the thrust. However, when using an oxidizer-to-fuel ratio this high, it can quickly corrode the rocket nozzle and induce unstable burning. To achieve stable ratios of oxidizer-to-fuel, the solid fuel, which is normally manufactured in a cylindrical fashion on its inner surface, is fabricated with very long length-to-diameter ratios to increase the total burning area. These high aspect ratios produce higher thrust, but poor volumetric efficiency, and a potential for lateral structural loading issues during high thrust burns. In place of traditional cylindrical fuel ports, it is proposed that by researching the effects of a helical fuel port structure, a significant increase in fuel burning rates can be observed. The benefits of increasing volumetric efficiencies by lengthening the internal flow path will also be observed. This increased fuel burning rate is due to two mechanisms inherent in the design of this helical fuel port. They are driven by the increased friction of the oxidizer against the solid fuel surface and the reduction of the effect of the burning fuel

pushing the flame away from the fuel surface. Preliminary results have been obtained using additive manufacturing to fabricate hybrid rocket fuel grains from acrylonitrile-butadiene-styrene (ABS). The burn-rate amplifications due to helical fuel port structures have been observed to be up to 3.0x than that of cylindrical fuel ports.

Contents

	Page
Abstract	iii
Public Abstract	v
List of Tables	ix
List of Figures	x
Acronyms	xii
1 Introduction	1
1.1 Increasing Fuel Mass Flow Rates in Hybrid Motors with Compact Form Factors	1
1.2 Hybrid Fuel Regression Rate Enhancement Techniques	3
1.3 Disadvantages of Current Thermosetting Polymer Materials as Hybrid Rocket Fuels	5
1.4 Acrylonitrile Butadiene Styrene (ABS) as a Potential Hybrid Rocket Fuel Material	6
2 Hybrid Regression Rate Theory	10
2.1 Hybrid Fuel Regression Rate Mechanism Overview	10
2.2 Estimating the Skin Friction Coefficient for Hybrid Rocket Fuel Port Flow .	13
2.3 Effect of Ablated Fuel Massflow on Fuel Regression Rate	15
3 Helical Effects	18
3.1 Effects of Helical Fuel Port on Regression Rate	18
3.2 Helical Regression Rate Model Development	20
3.2.1 Skin Friction Amplification Factor	20
3.2.2 Radial Blowing Suppression Amplification Factor	22
4 Experimental Verification of Helix Amplification Factors	24
4.1 Test Apparatus for GOX-ABS Motor Tests	24
4.2 Fuel Grains and Assembly	26
4.3 Results	30
4.3.1 Measured Regression Rate	30
4.3.2 Amplification Factors	32
4.3.3 Effect of Rotational Reynolds Number	32
4.3.4 Volumetric Efficiency	34
4.3.5 Optimal O/F Shift	37
5 Conclusion	40
5.0.6 Future Work	41

References **44**

List of Tables

Table	Page
4.1 Tested Fuel Port Parameters	29

List of Figures

Figure	Page
1.1 Example of a Multi-Port-Style Fuel Grain	2
1.2 Example of a Swirl-Injector Setup	4
1.3 Fuel Grain Manufactured using Cast and Cure Techniques	7
1.4 Monomers in ABS Polymer,	8
2.1 Enthalpy Balance Model for Hybrid Fuel Regression Rate	12
3.1 Helical Coil,	18
3.2 Helix Parameters,	19
3.3 Short-Pitch, Fuel Port Cross-Sections For Three Different Mean Regression Values.	22
4.1 KRMT Test Stand P&ID	25
4.2 Motor Installed on KRMT Test Stand	25
4.3 Stratasys Dimension 1200es 3-D FDM Printer	27
4.4 Statasys Printer Simultaneously Building Multiple Fuel Grain Segments . .	28
4.5 Assembled 3d-printed Fuel Grain with Interlocking Segments	28
4.6 Schematic of Lab Scale Hybrid Motor with Snap Together Helical Fuel Grains	29
4.7 Assembled 75-mm Motor Firing in Test Cell	29
4.8 Post-Test Fuel Grain Cross Sections	31
4.9 GOX-ABS Regression Rate Data and Model Comparison for Straight-Bore and Helical Grains	33
4.10 Predicted Regression Rate Amplification Factors for Helical Fuel Ports . . .	33
4.11 Predicted O/F Ratios and Characteristic Velocity for Helical Fuel Ports . .	34
4.12 Effect of Rotational Reynolds Number on Fuel Regression Rate	35

4.13 Long vs. Short Grain Thrust Curve Comparison	35
4.14 Long vs. Short Grain Length Efficiency Comparison	36
4.15 O/F Ratios vs Oxidizer Massflux	38
4.16 NASA Armstrong Throttled Hybrid Rocket Motor	39
4.17 Cross-Section of Throttled Hybrid Motor Case	39
5.1 Aggressive Helical Fuel Port Pre-Burn Visualization	43
5.2 Aggressive Helical Fuel Port Post-Burn Visualization	43

Acronyms

ABS	acrylonitrile butadiene styrene
HTPB	hydroxyl-terminated polybutadiene
FDM	fused deposition modeling
USU	Utah State University
GOX	gaseous oxygen
KRMT	kart for reactive monopropellant testing
P& ID	plumbing and instrumentation diagram
HAN	hydroxylammonium nitrate
O/F	oxidizer to fuel
PBAN	polybutadiene acrylonitrile
GAP	glycidyl azide polymer
ESOH	environmental safety and occupational health risks
N ₂ O	nitrous oxide
Isp	specific impulse
CNC	computer numerically controlled

Nomenclature

α	Scaling Constant
\bar{G}_{ox}	Mean Longitudinal Oxidizer Massflux
β	Blowing Effect
$\Delta h_{fuel\ surf}$	Specific Enthalpy of Convection from Flame Zone to Fuel Surface
δ_x	Local Boundary Layer Thickness
\dot{r}	Fuel Linear Regression Rate
$\bar{\dot{r}}$	Mean Longitudinal Fuel Regression Rate
η	Chamber Pressure Length Efficiency
$(C_{f_x})_{blowing}$	Blowing Corrected Skin Friction Coefficient
μ	Dynamic Viscosity
$\rho_e U_e \sim G_{ox}$	Oxidizer Massflux at the Edge of the Boundary Layer
A_β	Helical Amplification Factor due to Blowing Effect Suppression
A_{burn}	Fuel Burning Surface Area
A_{C_f}	Helical Amplification Factor due to Increased Surface Friction
A_c	Fuel Port Cross Sectional Area
B'	Corrected Blowing Effect Coefficient
\bar{D}	Mean Longitudinal Fuel Port Diameter
$C_{f_{helix}}$	Straight Tube Skin Friction Coefficient
$C_{f_{straight}}$	Helical Coil Skin Friction Coefficient
C_{f_x}	Local Skin Friction Coefficient
D	Fuel Port Diameter
d	Helix Diameter
$D(x)$	Local Fuel Port Diameter
\dot{m}_{prop}	Fuel Massflow rate
$F_{blowing}$	Blowing Effect Force
F_c	Centrifugal Force

G_{ox}	Oxidizer Mass Flux
h_v	Enthalpy of Vaporization
L	Fuel Port Length
L_{long}	Fuel Grain No. 1 Fuel Grain Length
L_{short}	Fuel Grain No. 6 Fuel Grain Length
N	Number of Helical Rotations
P	Helix Pitch
P_o	Stagnation/Chamber Pressure
P_{long}	Fuel Grain No. 1 Chamber Pressure
P_r	Turbulent Prandtl Number
P_{short}	Fuel Grain No. 6 Chamber Pressure
r	Helix Radius
r_0	Initial Fuel Port Radius
$R_{c_{effective}}$	Effective Helix Radius of Curvature
R_c	Helix Radius of Curvature
$R_{e\omega}$	Rotational Reynolds Number
R_{e_x}	Local Reynolds Number
R_h	Helix Ratio
ρ_{ox}	Oxidizer Density
ρ_{prop}	Fuel Density
S	Run-Length of Helical Centerline
s	Fuel Port Linear Regression
S_t	Stanton Number
V_{ox}	Velocity of Massflux at edge of Oxidizer Boundary Layer
V_w	Velocity of Massflux Emanating from Fuel Surface
x	Fuel Port Local Position

Chapter 1

Introduction

Hybrid rocket motors, in spite of their well-known safety and handling advantages [1], have not seen widespread commercial use due to internal motor ballistics [2] that produce fuel regression rates typically 25-30% lower than solid fuel motors in the same thrust and impulse class. These lowered fuel regression rates tend to produce unacceptably high oxidizer to fuel (O/F) ratios that lead to potential combustion instability, erosive burning, and nozzle erosion, which all lead to highly reduced motor duty cycles. To achieve O/F ratios that produce acceptable combustion characteristics in hybrid rocket motors, traditional cylindrical fuel ports have been fabricated to have a very long length to diameter ratio. This high aspect ratio results in poor volumetric efficiency and presents the potential for lateral structural loading issues in the motor during high thrust burns.

1.1 Increasing Fuel Mass Flow Rates in Hybrid Motors with Compact Form Factors

Increasing the oxidizer mass flux can theoretically increase fuel regression rates; unfortunately, the resulting combustion instabilities at high flux rates limit the effectiveness of this option [3]. These high flux rates also drive the oxidizer to fuel (O/F) ratio far from the stoichiometric point of combustion, vastly reducing the efficiency of the motor. To achieve enhanced fuel mass flows for oxidizer mass flux levels that produce highly efficient and stable combustion, hybrid fuel grain designers have resorted to increasing the fuel grain surface burn area by casting multiple fuel ports with a large pre-combustion chamber or multiple injectors (see Fig. 1.1). The original AMROC 15-port grain design is a classic realization of this technique [4]. However, this multiple port approach presents several disadvantages [5].

First, the overall fuel regression rate is reduced as the number of ports increases due



Fig. 1.1: Example of a Multi-Port-Style Fuel Grain

to the drop in oxidizer mass flux and the motor diameter size grows accordingly. Second, a significant potential for uneven port burning exists, producing an excessive un-burned mass fraction (usually greater than 10%). Uneven burning presents a significant potential for compromised fuel grain integrity, especially towards the end of the burn. Un-burned fuel slivers can potentially break off the fuel grain and throw chunks out the back of the rocket. These large pieces of material could easily build up inside the nozzle of the rocket, resulting in a catastrophic failure of the motor casing. Third, multiple port designs present an increased risk of motor instability related to dynamic flow interactions between ports and/or the presence of a large pre-combustion chamber. Fourth, complex multi-port geometries require the development of extensive tooling, and the current method of manufacturing multi-port fuel grains present an unavoidable difficulty with removing the tooling once the grain material is set. Fifth, a requirement for an embedded structure to support the fuel port as it regresses is often required in multi-port designs. The presence of this web adds to the un-burned mass fraction for the motor and creates a difficult material science problem of keeping the web intact in stagnation temperatures exceeding 3000 C.

1.2 Hybrid Fuel Regression Rate Enhancement Techniques

Although techniques generally based on increasing the heat transfer from the combustion zone to the fuel grain surface have been tested, most of these methods suffer significant operational shortcomings. These techniques include adding oxidizing agents to the fuel material [6], adding metal particles to the fuel grain [4], and the using swirl injection to increase the local oxidizer surface mass flux [7] (See Fig. 1.2).

All of these techniques demonstrate some ability to enhance regression rates, but also introduce multiple disadvantages. Introducing oxidizing materials into the fuel grain weakens the fuel material which may introduce a pressure-coupling instability during the motor burn. The result is a significantly increased explosion risk. Introducing micron-sized metal particles can also introduce pressure coupling, and the resulting increase in the effective molecular weight of the exhaust product results in only marginal end-to-end motor performance improvements. Introducing nano-sized metal particles dramatically increases motor production costs, and uniform fuel grain material properties are extremely difficult to achieve. Finally, introducing swirl injection significantly increases motor costs, requires heavy injectors or vanes, and is subject to scaling limitations for large-scale motors.

Others have tried to avoid adding materials to their fuel by changing to a fuel which provides a higher regression rate. Karabeyoglu, et al. [8], recently investigated a class of hybrid fuel grain materials based on a paraffin wax formulation. These paraffin-based fuels melt before vaporizing, and a properly formulated wax mix produces a melt layer with a low viscosity and high surface tension. When the oxidizer flows at high speed over the upper side of the melting fuel surface, the liquid layer becomes unstable and minute surface waves form. The resulting fluid boundary layer is hydro-dynamically unstable and allows fuel droplets to be entrained into the core flow. The entrained fluid droplets significantly increase the mass flow generated by the ablating fuel, but does not increase the "blowing-effect" regression rate suppression resulting from the ablating radial mass flow. For stable oxidizer flux levels droplet entrainment mass flow is significantly greater than mass flow resulting from direct gasification. Paraffin-based fuels have been proven to burn at surface regression rates three

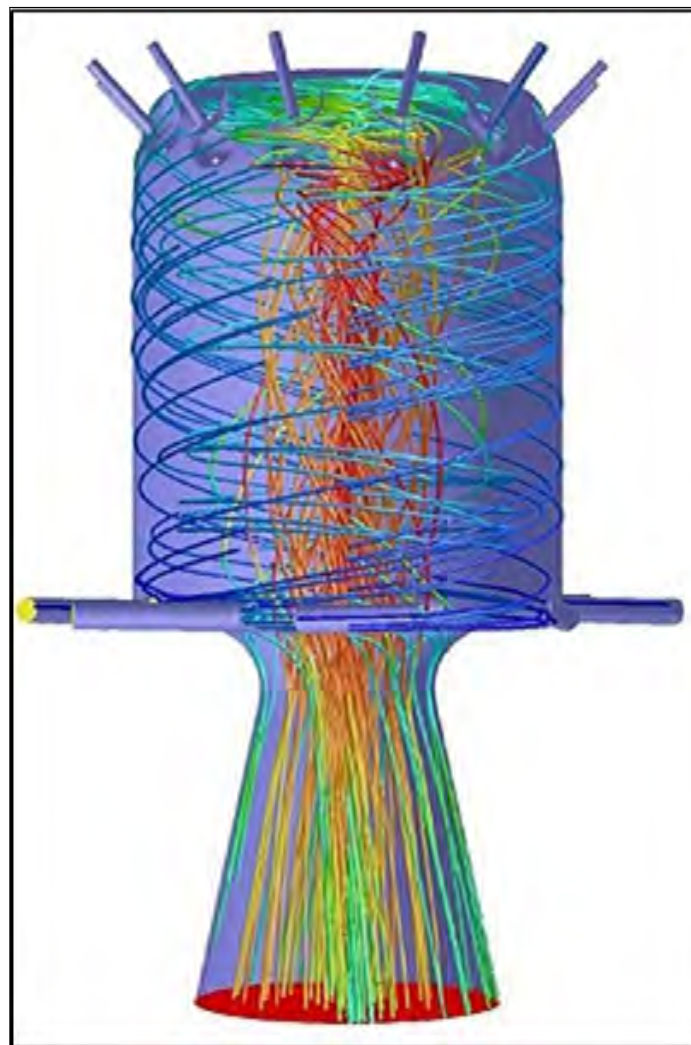


Fig. 1.2: Example of a Swirl-Injector Setup

to four times that of conventional hybrid fuels [9]. These high regression rates remove the need for a complex multi-port grain, and most applications can be designed with a single port configuration with this fuel. Karabeyoglu, et al. have ground-tested paraffin fuel hybrid rocket motors as large as 60 cm in diameter [10]. However, due to the fuel drop entrainment, significant unburned materials are ejected from the nozzle, and combustion efficiencies for paraffin-based fuels are inherently lower. More significantly, the properties that allow the fuel droplet entrainment in paraffin-based fuels introduce mechanical and structural problems that reduce the fuel grain integrity as the propellant burns. Paraffin in its solid phase is rather brittle and easily cracks when subjected to launch vibration loads. As the paraffin melts, the material softens and tends to flow and “sluff” off the fuel surface under axial launch loads. Thus, paraffin-based fuels require either special additives or a support lattice to keep the grain structure intact under launch loads.

Several additives have been tested in hybrid motors to strengthen the fuel material [11], aiming to avoid using embedded support structures in the fuel. Polyurethane foam (PUF) strengthening structure shows promising results, but leads to heterogeneous fuel formulations. These heterogeneous grain structures are difficult to manufacture. To avoid this problem and ensure paraffin-based formulations with sufficient elasticity to survive launch vibration levels, a miscible thermoplastic elastomer, Styrene-Ethylene-Butylene-Styrene (SEBS), was tested as a strengthening alternative to PUF. Mixing SEBS into the paraffin fuel produces a homogenous fuel grain and offers significantly lower manufacturing costs. During the combustion of the homogeneous material the material melts; when using heterogeneous materials, only the paraffin melts. In both cases, SEBS fuel additive and PUF structural support materials reduced the burn effectiveness and performance of the hybrid motor.

1.3 Disadvantages of Current Thermosetting Polymer Materials as Hybrid Rocket Fuels

The vast majority of conventional hybrid rocket motor designs use isocyanate-cured polymers Hydroxyl-Terminated Polybutadiene (HTPB), Polybutadiene Acrylonitrile (PBAN), and Glycidyl Azide Polymer (GAP) as the fuel grain material. These fuels are legacy materi-

als derived from solid propellant and explosive ordnance manufacture. The US Department of defense considers these materials to be environmentally unsustainable for large-scale propellant production and is actively seeking replacement alternatives [12]. The isocyanate curatives present a wide variety of Environmental Safety and Occupational Health risks (ESOH) including irritation of the skin, mucous membranes, eyes, and respiratory tract; contact and allergic dermatitis; hypersensitivity pneumonitis; and respiratory sensitization. Some studies have demonstrated that isocyanates also exhibit carcinogenic and detrimental reproductive effects.

These thermosetting propellants all use a labor intensive “cast and cure” method for producing hybrid fuel grains, and high production rates cannot be achieved without a significant manufacturing infrastructure (See Fig. 1.3).

These binder materials are mixed from liquid base components, degassed under vacuum, and then cast and cured in a fuel grain mold. This labor-intensive manufacture and assembly approach results in market-prohibitive production costs and cannot produce the quantity and varieties of motors required to support the ambitious launch rates necessary to support what is expected to be a fast-growing commercial space industry. Most significantly for the current research effort, thermosetting polymers materials do not melt in the presence of heat, but instead char and ablate. Once set, they cannot be remanufactured into another component or recycled. Because the base materials must be cast and cured using tooling and mandrels to set the port geometries, there are limitations to the types of port geometries that can be developed. With the exception of pre and post-combustion ports, achievable cure geometries are restricted to axi-symmetric designs with identical port cross sections at each longitudinal station.

1.4 Acrylonitrile Butadiene Styrene (ABS) as a Potential Hybrid Rocket Fuel Material

Whitmore, and Peterson [13] at Utah State University, have recently investigated the use of ABS thermoplastic as a hybrid rocket fuel material. A key outcome of this research was the demonstration of the thermodynamic equivalence of ABS to traditionally-



Fig. 1.3: Fuel Grain Manufactured using Cast and Cure Techniques

used HTPB when burned with nitrous oxide (N_2O). In a series of comparison tests, it was discovered that combustion flame temperature for N_2O/ABS is slightly cooler than $N_2O/HTPB$, but the products of combustion have a lower molecular weight. Thus, ABS achieves specific impulse (Isp) and characteristic velocity (C^*) that are nearly identical to HTPB. ABS and HTPB fuel regression rates for cylindrical fuel ports were measured to be nearly identical. However, when compared to thermoset materials such as HTPB, ABS has several mechanical properties that make it very attractive as a hybrid rocket fuel. ABS is an inexpensive thermoplastic material that is widely mass-produced for a variety of non-combustion applications including household plumbing and structural materials. More than 1.4 billion kilograms of ABS material were produced by petrochemical industries world-wide in 2010 [14]. ABS is 100% recyclable and can be reshaped multiple times with little or no degradation of the material properties. ABS [15] is manufactured by co-polymerizing acrylonitrile and styrene to form styrene-acrylonitrile (SAN). Butadiene is then dissolved into the SAN to create ABS. Typical ABS preparations contain 21%-27% acrylonitrile, 12%-25% butadiene, and 54%-63% styrene. Acrylonitrile improves ABS's overall chemical resistance, butadiene imparts impact resistance, and styrene supplies good processability and stiffness.

It must also be noted that ABS has very high tensile strength of 40 MPa, compared to a maximum of 800 kPa for conventionally cured HTPB [16]. In fact, the yield strength of

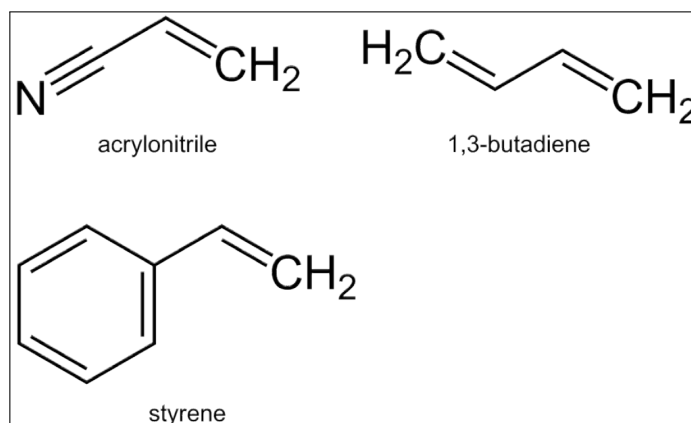


Fig. 1.4: Monomers in ABS Polymer,

conventional ABS stock is approximately 38% of that of aluminum. This material robustness makes ABS impervious to grain fracture, and very small grain features will retain a high structural strength. The relative strength of the ABS fuel material may allow the fuel grain to take a significant portion of the combustion chamber radial pressure load and may serve to reduce the wall thickness requirements for the motor case.

This strength of ABS is advantageous for fuel structures that are not possible in HTPB due to HTPB's poor structural strength. This strength also brings with it another advantage that can be applied in the manufacturing process of ABS fuel grains. ABS is a non-crystalline material with an amorphous structure. As such, ABS does not possess a true melting point, but exists in a highly "softened" semi-fluid state before vaporizing. This fluid state exists over a wide temperature range that varies from 100 oC to 140 oC [17]. This property makes ABS the material of choice for a modern form of additive manufacturing known as Fused Deposition Modeling (FDM). In FDM, a plastic filament is unwound from a coil and supplies material to an extrusion nozzle. The nozzle is heated to melt the material and can move in both the horizontal and vertical directions by a computer numerically controlled (CNC) mechanism. Exploiting the FDM fabrication process for ABS offers the potential to revolutionize the manufacture of hybrid rocket fuel grains. FDM can support high production rates and can potentially improving hybrid fuel grain quality, consistency, and performance, while reducing development and production costs. Most significantly, us-

ing additive manufacturing, ABS fuel grains can be fabricated with an almost infinite range of fuel port shapes, allowing for significant enhancement of burn properties and combustion efficiencies [18]. Bath (2012) [19] at Utah State University investigated the 3D printing and burning of ABS fuel grains with complex port geometries and the development of software capable of modeling and predicting the regression of arbitrary cross sections. It is this manufacturing capability that will be exploited in the research to be detailed in this document. Specifically, the effects of helical port grain structures will be examined.

This document will serve to demonstrate the effectiveness of helical fuel ports to give an increase in regression rate of the base fuel material by a factor of up to 3.0, with an overall improvement in combustion efficiency and specific impulse. Fuller, et al. (2011) at Aerospace Corporation have also achieved success with burning helical structures that were fabricated using additive manufacturing techniques [18]. Arnold, et al. at Pennsylvania State University have also successfully tested additively manufactured hybrid rocket fuel grains with embedded swirl patterns [20]. The additive manufacturing process used by References [18] and [20] were stereo-lithography and not FDM.

Helical fuel grains, using ABS in additively manufactured grains, has the potential to solve many of the inherent problems with hybrid rocket motors. ABS plastic can be manufactured and stored safely, and can be recycled multiple times without significant material degradation. The production of fuel grains through additive manufacturing is also economical due to the ability to manufacture fuel grains with low-waste and without a large manufacturing infrastructure. With the addition of the volumetrically, and chemically efficient, helical fuel ports can these ABS fuel grains now compete with other current rocket technologies.

Chapter 2

Hybrid Regression Rate Theory

2.1 Hybrid Fuel Regression Rate Mechanism Overview

Two fundamentally different processes drive solid and hybrid fuel grain regression rates. Solid propellants are blended using a combination of oxidizer and fuel in a mass proportion that delivers the optimized performance for a given mission requirement. Because the propellant mixture ratio is set by the homogeneous propellant formulation, the O/F remains constant throughout the burn. Also, solid-propellant combustion occurs in a very thin zone near the fuel surface. The rate of regression is driven primarily by chemical kinetics and is directly coupled to the combustion chamber pressure through the well-known Saint Robert's law.

$$\dot{r} = a \cdot P_0^n \quad (2.1)$$

In Eq. 2.1, \dot{r} is the fuel regression rate normal to the fuel surface, P_0 is the combustion chamber pressure, and the parameters $\{a, n\}$ are Saint Robert's burn constants that are a function of the propellant formulation, density, level of metallization, and oxidizer grain size. The propellant mass flow generated by combustion is

$$\dot{m}_{prop} = A_{burn} \cdot \rho_{prop} \cdot \dot{r} \quad (2.2)$$

In Eq. 2.2, A_{burn} is the burning surface area, and ρ_{prop} is the propellant density. When coupled with the nozzle geometry and combustion properties for the specific propellant formulation, the operating chamber pressure directly influences the delivered motor thrust and impulse profile. Key factors in burn profile shaping for solid motors include the propellant burn exponent (n) and exposed surface area-to-port volume as the fuel grain burns.

In contrast to solid rocket motors regression rate, hybrid fuel regression rates have little or no dependence on chamber pressure. Thus, hybrid fuel regression rate models based on St. Robert's law are inaccurate. Studies by Marxman and Gilbert [21] demonstrate that combustion processes for hybrid rockets are mostly driven by the boundary layer fluid mechanics where fuel regression rate is a result of turbulent boundary-layer heat transfer. Fuel regression rate is strongly correlated with the oxidizer massflow through the combustion chamber. Marxman and Gilbert posed a length-dependent "Saint-Roberts" type empirical regression rate model, where the oxidizer massflux replaces the chamber pressure.

$$\dot{r}_x = \frac{a \cdot G_{ox}^n}{x^m} \quad (2.3)$$

In Eq. 2.3, G_{ox} is the oxidizer massflux, x is the longitudinal location within the fuel port, and $\{a,n,m\}$ are empirical constants. The initial studies performed by Marxman and Gilbert predict values for $n \approx 0.8$, and $m \approx 0.2$. The values of $n=0.8$ and $m=0.2$ agree well with hybrid rocket combustion data collected with nitrous oxide (N₂O) and HTPB as propellants.

Later Marxman et al. [22] proposed an enthalpy-based regression-rate model in which the convective heat transfer from the combustion flame layer is balanced by the energy of ablation of the fuel grain surface.

$$\rho_{fuel} \cdot \dot{r} \cdot h_v = S_t \cdot \rho_e \cdot U_e \cdot \Delta h_{fuel_{surf}} \quad (2.4)$$

In Eq. 2.4, \dot{r} is the linear regression rate perpendicular to the fuel surface, $\Delta h_{fuel_{surf}}$ is the convective enthalpy transfer per unit massflow from the flame zone to the fuel surface, h_v is the enthalpy of vaporization (latent heat) of the fuel material, ρ_{fuel} is the density of the solid fuel material, S_t is the non-dimensional Stanton number, and $\rho_e U_e \sim G_{ox}$ is the oxidizer massflux at the edge of the boundary layer. In this model, radiation effects and heat conduction within the fuel grain are considered negligible. This is a fairly good assumption if ABS is used as fuel, as it is a good insulator.

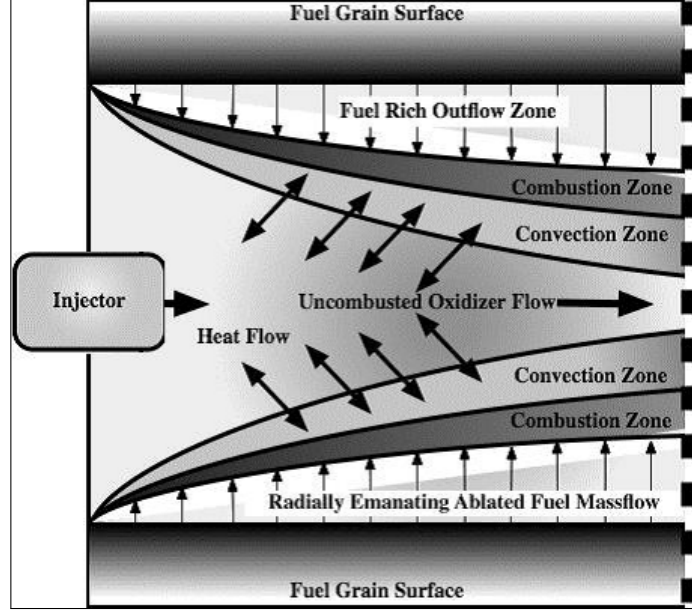


Fig. 2.1: Enthalpy Balance Model for Hybrid Fuel Regression Rate

The Stanton number can be written in terms of the local skin friction coefficient using the Reynold's-Coburn Analogy [23] [24] [25].

$$S_t = \frac{C_{f_x}}{2} \cdot P_r^{-\frac{2}{3}} \quad (2.5)$$

Substituting Eq. 2.5 into Eq. 2.4 the regression rate is written in terms of the local surface skin friction coefficient.

$$\dot{r} = \left(\frac{G_{ox}}{2P_r^{\frac{2}{3}}\rho_{fuel}} \right) \cdot \left(\frac{\Delta h_{fuel\ surf}}{h_v} \right) \cdot C_{f_x} \quad (2.6)$$

In Eqs. 2.5 and 2.6, C_{f_x} is the local skin friction coefficient, P_r is the non-dimensional turbulent Prandtl number, and G_{ox} is the oxidizer massflow per unit cross sectional area at the edge of the boundary layer.

Normally, boundary layer mixing would allow the oxidizer flow at the center of the fuel port to directly mix with vaporized material leaving the fuel wall. However, as shown by Figure 2.1, the radially emanating flow from the ablating fuel surface pushes the combustion zone away from the wall, reducing the effectiveness of the boundary layer mixing process

and insulating the convective heat transfer zone from the fuel grain surface. It is this radial “wall blowing” that is the primary cause for the low fuel regression rates typically observed in hybrid fuel combustion. The radial blowing effect also significantly reduces the local surface shearing stress.

Using Lees’ model [26] to account for the radially emanating flow field, Boardman [4] developed the correlation of Eq. 2.7 for the local surface skin friction coefficient in the presence of radial wall blowing.

$$\frac{(C_{f_x})_{blowing}}{C_{f_x}} = \frac{1.27}{\beta^{0.77}} \approx \frac{1.27}{\left(\frac{\Delta h_{fuel}}{h_v}\right)^{0.77}} \quad (2.7)$$

In Eq. 2.7, β is Lee’s “blowing coefficient” defined as the ratio of the massflux emanating from the surface to the massflux at the edge of the boundary layer (oxidizer) divided by one half of the skin friction coefficient

$$\beta = \frac{\rho_w \cdot V_w}{\rho_{ox} \cdot V_{ox} \cdot \frac{C_{f_x}}{2}} \quad (2.8)$$

Also in Eq. 2.7, C_{f_x} is the local skin friction without radial blowing, and $(C_{f_x})_{blowing}$ is the “blowing corrected” skin friction coefficient. For turbulent flow Boardman shows that the “blowing” coefficient is the thermodynamic equivalent of the non-dimensional enthalpy difference between the fuel surface and the flame zone and is equal to $\beta = \frac{\Delta h_{fuel}}{h_v}$. Allowing the blowing-corrected skin friction to substitute for the local skin friction coefficient, Eq. 2.1 results in the “blowing adjusted” regression rate model as a function of skin friction

$$\dot{r}_x = \frac{0.635 \cdot G_{ox}}{P_r^{\frac{2}{3}} \cdot \rho_{fuel}} \cdot \beta^{0.23} \cdot C_{f_x} = \frac{0.635 \cdot G_{ox}}{P_r^{\frac{2}{3}} \cdot \rho_{fuel}} \cdot \left(\frac{\Delta h_{fuel}}{h_v}\right)^{0.23} \cdot C_{f_x} \quad (2.9)$$

2.2 Estimating the Skin Friction Coefficient for Hybrid Rocket Fuel Port Flow

Eilers and Whitmore [27] show that Marxman’s empirical regression rate parameter

values $\{n = 0.8, m = 0.2\}$, can be directly derived by assuming the Blasius formula for turbulent wall shear stress, [24]

$$C_{f_x} = \frac{\tau_{wall_x}}{\frac{1}{2} \cdot \rho \cdot U_e^2} = \frac{0.0465}{(R_{e_x})^{\frac{1}{4}}} = \frac{0.0465}{\left(\frac{\rho \cdot U_e \cdot \delta_x}{\mu}\right)^{\frac{1}{4}}} \quad (2.10)$$

and using the empirically-derived Schlichting [28] model for turbulent boundary layer thickness

$$\delta_x = \frac{0.38x}{(R_{e_x})^{\frac{1}{5}}} = \frac{0.38x}{\left(\frac{\rho \cdot U_e \cdot x}{\mu}\right)^{\frac{1}{5}}} \quad (2.11)$$

In Equations 2.10 and 2.11, R_{e_x} is the local Reynolds number based on length at longitudinal station x downstream of the injector, δ_x is the local boundary layer thickness, and μ is the dynamic viscosity of the fluid. Substituting 2.11 into 2.10 and rearranging derives the Schoenherr-Schlichting skin friction model

$$C_{f_x} = \frac{0.0592}{(R_{e_x})^{\frac{1}{5}}} = \frac{0.0592}{\left(\frac{\rho_e \cdot U_e \cdot x}{\mu}\right)^{\frac{1}{5}}} = \frac{0.0592}{\left(\frac{G_{ox} \cdot x}{\mu}\right)^{\frac{1}{5}}} \quad (2.12)$$

When Eq. 2.12 is substituted into Eq. 2.1, the Marxman parameter values are derived.

$$\dot{r}_x = \frac{0.635 \cdot G_{ox}}{P_r^{\frac{2}{3}} \cdot \rho_{fuel}} \cdot \left(\frac{\Delta h_{fuel}}{h_v}\right)^{0.23} \cdot \frac{0.0592}{G_{ox}^{\frac{1}{5}}} \cdot \left(\frac{\mu}{x}\right)^{\frac{1}{5}} = \frac{0.0376 \cdot \mu^{\frac{1}{5}}}{P_r^{\frac{2}{3}} \cdot \rho_{fuel}} \cdot \left(\frac{\Delta h_{fuel}}{h_v}\right)^{0.23} \cdot \left(\frac{G_{ox}^{\frac{4}{5}}}{x^{\frac{1}{5}}}\right) \quad (2.13)$$

Empirical observations have shown that depending on the propellants used, the regression rate exponent n is not exactly as predicted by the Marxman model; instead n tends to range between 0.3 to 0.8 with m approximately equal to $1-n$. Values less than $n = 0.3$ or greater than $n = 0.8$ are not typically observed [29]. Eq 2.13 can be generalized by replacing the “4/5” exponent by n , letting $m = 1 - n$, and allowing an additional scaling constant α , whose value is approximately 1.

$$\dot{r}_x = \alpha \cdot \left(\frac{0.0376 \cdot \mu^{1-n}}{P_r^{\frac{2}{3}} \cdot \rho_{fuel}} \right) \cdot \left(\frac{\Delta h_{fuel}}{h_v} \right)^{0.23} \cdot \left(\frac{G_{ox}^n}{x^{1-n}} \right) \quad (2.14)$$

In order to calculate a more computationally-friendly average regression rate, a mean longitudinal diameter will first need to be approximated by integrating the local port diameter $D(x)$ along the length of the fuel port.

$$\bar{D} = \frac{1}{L} \int_0^L D(s) ds \quad (2.15)$$

Eq. 2.14 can then also be integrated along the length of the port to approximate the longitudinal mean of the fuel regression rate.

$$\bar{r} = \frac{1}{L} \int_0^L \alpha \left(\frac{0.0376 \cdot \mu^{1-n}}{P_r^{\frac{2}{3}} \cdot \rho_{fuel}} \right) \cdot \left(\frac{\Delta h_{fuel}}{h_v} \right)^{0.23} \cdot \left(\frac{G_{ox}^n}{x^{1-n}} \right) dx = \frac{\alpha}{n} \cdot \left(\frac{0.0376 \cdot \mu^{1-n}}{P_r^{\frac{2}{3}} \cdot \rho_{fuel}} \right) \cdot \left(\frac{\Delta h_{fuel}}{h_v} \right)^{0.23} \cdot \left(\frac{\bar{G}_{ox}^n}{L^{1-n}} \right) \quad (2.16)$$

In Eq. 2.16, \bar{G}_{ox} is the longitudinal mean of the oxidizer massflux. Using the Marxman value of $n=0.8$ as the burn exponent and assuming the scaling parameter α to be unity, Eq. 2.16 reduces to the form published by Eilers and Whitmore.

$$\bar{r} = \left(\frac{0.047 \cdot \mu^{\frac{1}{5}}}{P_r^{\frac{2}{3}} \cdot \rho_{fuel}} \right) \cdot \left(\frac{\Delta h_{fuel}}{h_v} \right)^{0.23} \cdot \left(\frac{\mu}{L} \right)^{\frac{1}{5}} \cdot \bar{G}_{ox}^{\frac{4}{5}} \quad (2.17)$$

2.3 Effect of Ablated Fuel Massflow on Fuel Regression Rate

When properly calibrated with the appropriate burn exponent and scaling constant $\{n, a\}$ for a given propellant combination, Eq. 2.14 has been shown to accurately predict the mean longitudinal regression rate for hybrid rockets using propellants with a high nominal O/F ratio. This kind of behavior can be found in the traditional nitrous oxide and HTPB motors [30] where the best operating O/F = 6. For hybrid rockets using propellants with relatively lower O/F ratios, the ablated fuel massflux contributes significantly to the total

port skin friction and the oxidizer massflux is replaced with the total massflux at each cross section of the port.

$$\dot{r}_x = \frac{a \cdot G_{total}^n}{x^m} \quad (2.18)$$

For a cylindrical port the total massflux is

$$G_{total} = \frac{\dot{m}_{ox} + \dot{m}_{fuel}}{A_c} = \frac{\rho_{fuel} \cdot \int_0^x C_{port} \cdot \dot{r}(s) ds}{A_c} = G(x)_{ox} + \frac{4 \cdot \rho_{fuel} \cdot \int_0^x D(s) \cdot \dot{r}(s) ds}{D(x)^2} \quad (2.19)$$

Replacing the local port diameter $D(x)^2$ by the longitudinal average port diameter from Eq. 2.15, substituting into Eq. 2.19, and differentiating with respect to x results in

$$\frac{\partial G_{total}}{\partial x} = \frac{4 \cdot \rho_{fuel} \cdot a \cdot x^{-m}}{\bar{D}}. \quad (2.20)$$

Separation of variables results in

$$\int_{G_0}^{G_x} \frac{1}{G_{total}} \cdot \partial G_{total} = \int_0^x \frac{4 \cdot \rho_{fuel} \cdot a \cdot x^{-m}}{\bar{D}} \partial x. \quad (2.21)$$

Since no ablated fuel has accumulated in the port at $x = 0$, the total massflux at the port inlet equals the oxidizer massflux, and Eq. 2.21 is integrated from the port inlet to station x to give the result

$$G(x)^{1-n} = G_{ox}^{1-n} + \left(\frac{1-n}{1-m} \right) \cdot \frac{4 \cdot \rho_{fuel} \cdot a \cdot x^{1-m}}{\bar{D}}. \quad (2.22)$$

Eq. 2.22 is integrated along the length of the port and divided by the port length to give the mean longitudinal value for the total massflux.

$$\bar{G}_{total} = \left[\bar{G}_{ox}^{1-n} + \left(\frac{1-n}{(1-m) \cdot (2-m)} \right) \frac{4 \cdot \rho_{fuel} \cdot a}{\bar{D}} \cdot L^{1-m} \right]^{\frac{1}{1-n}} \quad (2.23)$$

Replacing G_{ox} in Equation 2.16 by the total mean massflux as calculated by Eq. 2.23 gives

$$\bar{r} = \frac{\alpha}{n} \cdot \left(\frac{0.0376}{P_r^{\frac{2}{3}} \cdot \rho_{fuel}} \right) \cdot \left(\frac{\Delta h_{fuel}}{h_v} \right)^{0.23} \cdot \left(\frac{\mu}{L} \right)^{1-n} \cdot \left[\bar{G}_{ox}^{1-n} + \left(\frac{1-n}{(1-m) \cdot (2-m)} \right) \cdot \frac{4 \cdot \rho_{fuel} \cdot a}{\bar{D}} \cdot L^{1-m} \right]^{\frac{n}{1-n}}. \quad (2.24)$$

Inspection of Eqs. 2.16 and 2.17 shows that

$$a = \frac{\alpha}{n} \cdot \left(\frac{0.0376}{P_r^{\frac{2}{3}} \cdot \rho_{fuel}} \right) \cdot \left(\frac{\Delta h_{fuel}}{h_v} \right)^{0.23} \cdot \mu^{1-n}. \quad (2.25)$$

Substituting Eq. 2.25 into Eq. 2.24 and simplifying gives

$$\bar{r} = \frac{\alpha}{n} \cdot \left(\frac{0.0376}{P_r^{\frac{2}{3}} \cdot \rho_{fuel}} \right) \cdot \left(\frac{\Delta h_{fuel}}{h_v} \right)^{0.23} \cdot \left(\frac{\mu}{L} \right)^{1-n} \cdot \left[\bar{G}_{ox}^{1-n} + \left(\frac{(1-n) \cdot \left(\frac{4\alpha}{n} \right)}{(1-m) \cdot (2-m)} \right) \cdot \left(\frac{0.0376}{P_r^{\frac{2}{3}}} \right) \cdot \left(\frac{\Delta h_{fuel}}{h_v} \right)^{0.23} \cdot \left(\frac{\mu^{1-n}}{\bar{D} L^{1-m}} \right) \right]^{\frac{n}{1-n}}. \quad (2.26)$$

Substituting the classical Marxman burn parameters $\{n = 4/5, m = 1/5\}$ and assuming *alpha* equal to unity, Eq. 2.26 reduces to the relatively simple expression that accounts for the effects of the mean longitudinal fuel massflux on the fuel regression rate.

$$\bar{r} = \left(\frac{0.047}{P_r^{\frac{2}{3}} \cdot \rho_{fuel}} \right) \cdot \left(\frac{\Delta h_{fuel}}{h_v} \right)^{0.23} \cdot \left(\frac{\mu}{L} \right)^{\frac{1}{5}} \cdot \left[\bar{G}_{ox}^{\frac{1}{5}} + \frac{5}{9} \cdot \left(\frac{0.047}{P_r^{\frac{2}{3}} \cdot \rho_{fuel}} \right) \cdot \left(\frac{\Delta h_{fuel}}{h_v} \right)^{0.23} \cdot \left(\frac{\mu}{L} \right)^{\frac{1}{5}} \cdot \frac{L}{\bar{D}} \right]^4 \quad (2.27)$$

Interestingly, based on the result of Eq. 2.27, approximately 5/9 or 56%, of the total ablated fuel massflow contributes to the mean longitudinal regression rate. Intuitively, this result makes sense because a greater fuel massflow is produced by the downstream port than the upstream port section; thus biasing the mean fuel massflow downstream of the longitudinal half-way point.

Chapter 3

Helical Effects

3.1 Effects of Helical Fuel Port on Regression Rate

Looking back at Eq. 2.1

$$\dot{r}_x = \frac{0.635 \cdot G_{ox}}{P_r^{\frac{2}{3}} \cdot \rho_{fuel}} \cdot \beta^{0.23} \cdot C_{f_x} = \frac{0.635 \cdot G_{ox}}{P_r^{\frac{2}{3}} \cdot \rho_{fuel}} \cdot \left(\frac{\Delta h_{fuel}}{h_v} \right)^{0.23} \cdot C_{f_x} \quad (3.1)$$

it's clear that the main passive contributors to the regression rate of the fuel are the skin friction (C_f) and the blowing effect (β). In order to significantly increase the fuel regression rate, any proposed port design feature must increase the nominal surface skin friction while also minimizing the effects of radial surface blowing. A helical fuel port structure serves this purpose. Helical fuel ports, in a wide variety of cross sectional areas, can be easily manufactured using ABS fuel materials manufactured by FDM techniques. It is well known that helical pipe flows have the effect of significantly increasing the local skin friction coefficient. Helical flows also introduce a centrifugal component into the flow field. In hybrid rocket applications, this centrifugal component will thin the wall boundary layer – bringing



Fig. 3.1: Helical Coil,

the flame zone closer to the wall surface and increasing the flame diffusion efficiency. The overall effect of this boundary layer thinning decreases the unwanted blowing effect.

The helical structure is defined by three parameters; the nominal fuel port diameter D , the helix loop diameter d , and the helix pitch length, P .

The pitch length is defined as the distance between the centerlines of two consecutive helical wraps. The pitch length is nominally calculated as the total length of the helix divided by the number of rotations along the length of the helix,

$$P = \frac{L}{N} \quad (3.2)$$

The total run-length of the helix centerline is

$$S = 2\pi \cdot N \cdot \sqrt{\left(\frac{d}{2}\right)^2 + \left(\frac{P}{2\pi}\right)^2} = 2\pi \cdot N \cdot \sqrt{r^2 + \left(\frac{P}{2\pi}\right)^2} \quad (3.3)$$

In Eq 3.3, r is the helix loop radius. In Eqs. 3.2 and 3.3, N is the number of rotations along the helix length. The radius of curvature of the helical arc is calculated from the loop diameter and pitch length as

$$R_c = \frac{d}{2} \cdot \left(1 + \left(\frac{P}{\pi \cdot d}\right)^2\right) = r \cdot \left(1 + \left(\frac{P}{2\pi \cdot r}\right)^2\right) \quad (3.4)$$

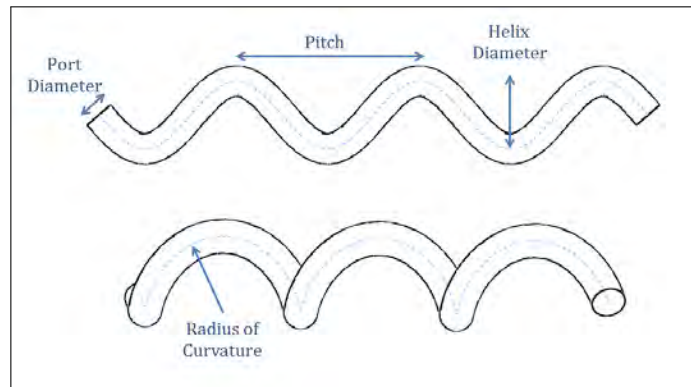


Fig. 3.2: Helix Parameters,

The helical fuel port ratio is defined as the helix diameter divided by the initial fuel port diameter $R_h = d/D_o$.

3.2 Helical Regression Rate Model Development

Clearly, based on Eq. 3.1, there two helical flow effects on the regression rate that must be modeled, 1) the effect of the helical flow upon the skin friction coefficient C_{f0} in the absence of wall blowing, and 2) the wall blowing suppression due to centrifugal force and the resulting decrease on β . The modified helical-flow regression rate model will be developed to take the form

$$\bar{r}_{helix} = \bar{r}_{straight} \cdot A_\beta \cdot A_{C_f} \quad (3.5)$$

Eq. 3.5 can be re-written terms of a total “amplification” factor on the nominal cylindrical port regression rate, calculated as the product of the individual amplification factors.

$$\frac{\bar{r}_{helix}}{\bar{r}_{straight}} = A_\beta \cdot A_{C_f} \quad (3.6)$$

A modified form of the Mishra-Gupta model developed by Whitmore [31] will be used to calculate the skin friction amplification factor, A_{C_f} . The Mishra-Gupta model will be modified to account for the increase in the effective centerline radius of curvature as the port burns, opens up, and becomes increasingly more cylindrical. The blowing suppression amplification factor A_β is modeled as a proportional ratio of the mean centrifugal force introduced by the helical flow to the momentum flow rate from the fuel surface caused by the ablating fuel material, $F_c/F_{blowing}$. The following sections detail the development of these models.

3.2.1 Skin Friction Amplification Factor

The skin friction amplification factor is developed from the extended turbulent flow correlation model to account for longer pitch lengths by replacing the coil radius with the radius of curvature of the helix, R_c . Mishra and Gupta investigated a wide range of coil

geometries for both laminar and turbulent flow conditions and derived a “universal” flow correlation of the form

$$C_{f_{helix}} = C_{f_{straight}} + 0.0075 \cdot \sqrt{\frac{D}{2R_c}} \quad (3.7)$$

$$C_{f_{straight}} = \frac{0.074}{(R_{e_L})^{\frac{1}{5}}} \quad (3.8)$$

Where $C_{f_{helix}}$ is the skin friction coefficient for the helical coil, $C_{f_{straight}}$ is the Schlichting approximation [28] of the longitudinal mean of the straight-bore skin friction coefficient, and $(R_{e_L})^{\frac{1}{5}}$ is the mean longitudinal Reynold’s number. For pipes with short pitch lengths, the Mishra and Gupta Model produces similar results to more commonly known models developed by White [32], Ito [33], and Gnielinski [34].

Considering the form of Eq. 3.8, it is reasonable to conclude that the growth in regression rate of the helical fuel port is proportional to growth in the end-to-end skin friction coefficient. This assumption is reasonably accurate for fuel ports with longer pitch; however, for ports with short pitch distances the helical loops “burn together” as the port opens up. Because of these merging helical loops, the port becomes more and more cylindrical with time and the radius of curvature grows rapidly. Fig. 3.3 illustrates this concept, where a short-pitch helical port cross section is shown for three different mean regression values, representing the fuel grain as the port burns and opens up. The plotted port cross-sections are for regression ratios, $s/R_c = \{0, 1.25, 2.5\}$. The symbol s is the linear regression of the fuel port calculated as the difference between the instantaneous and initial mean fuel port radius

Clearly, the final port cross section is no longer helical and the effective radius of curvature is nearly infinite. Here the helical effects on the surface skin friction are essentially zero. This time-dependent effect is approximately modeled by

$$R_{c_{effective}} = R_c \cdot \sqrt{1 + 2\pi \cdot \left(\frac{s}{R_c}\right)^2} = R_c \cdot \sqrt{1 + \frac{\pi}{2} \cdot \left(\frac{D - D_o}{R_c}\right)^2} \quad (3.9)$$

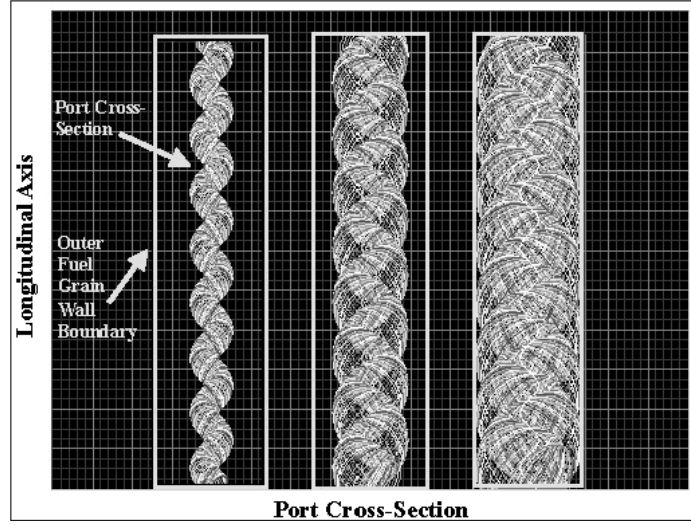


Fig. 3.3: Short-Pitch, Fuel Port Cross-Sections For Three Different Mean Regression Values.

In Eq. 3.9 $R_{c_{effective}}$ is the effective helical port radius of curvature, D is the instantaneous mean port diameter, D_o is the initial fuel port diameter, and R_c is the radius of curvature of the initial fuel port centerline. The calculated value for $R_{c_{effective}}$ replaces R_c in the Mishra-Gupta Model of Eq. 3.8 when calculating the skin friction amplification factor. The resulting formula is

$$A_{C_f} = \frac{C_{f_{straight}} + 0.0075 \cdot \sqrt{\frac{D}{2 \cdot R_{c_{effective}}}}}{C_{f_{straight}}} = 1 + \frac{0.0075}{C_{f_{straight}}} \sqrt{\frac{D}{2 \cdot R_c \cdot \sqrt{1 + \frac{\pi}{2} \left(\frac{D - D_o}{R_c} \right)^2}}} \quad (3.10)$$

3.2.2 Radial Blowing Suppression Amplification Factor

As described earlier in this section, the helical fuel port introduces a centrifugal flow component that pushes the flame zone closer to the inner grain boundary, increasing the heat transfer from the flame zone to the wall. This “blowing suppression” significantly increases the fuel regression rate and is proportional to the ratio of the helical-flow centrifugal force to the momentum flow of the radially-emanating fuel vapor at the inner wall boundary. The blowing suppression effect is approximated by

$$\beta' = \left(\frac{\beta}{1 + \frac{2 \cdot r / D}{\frac{\Delta h_{fuel} / h_v}{surf}}} \right) \quad (3.11)$$

In Eq. 3.11, B' is the blowing coefficient corrected for blowing suppression, r is the helical loop radius, D is the instantaneous mean fuel port diameter, and $\frac{\Delta h_{fuel} / h_v}{surf}$ is the enthalpy ratio based on the instantaneous mean oxidizer-to-fuel ratio (O/F). Rearranging Eq. 3.11, the regression rate amplification factor cause by blowing suppression is represented as

$$A_\beta = \left(1 + \left(\frac{d/D}{\frac{\Delta h_{fuel} / h_v}{surf}} \right) \right) \quad (3.12)$$

Chapter 4

Experimental Verification of Helix Amplification Factors

This section reports on a series of experiments that were conducted to verify the helical regression amplification factors as described above. During this testing campaign, a 75mm lab-scale motor was used to perform multiple test firings during which various additively manufactured helical ABS fuel port geometries were compared against a normal straight bore geometry. Gaseous oxygen (GOX) was used as the oxidizer.

4.1 Test Apparatus for GOX-ABS Motor Tests

To facilitate rapid evaluation of the proposed fuel port geometries, a custom mobile test stand, the Kart for Reactive Monopropellant Testing (KRMT), was developed. Fig. 4.1 displays a Piping and Instrumentation Diagram (P&ID) and a side view of the KRMT thrust stand, while Fig. 4.2 shows the motor installed on the test stand itself. The mobile cart was prepared for testing in the Propulsion Test Laboratory's development bay, and then moved to the secure test cell for test firings. The KRMT's instrumentation and controls suite was managed via a National Instruments Compact RIO with an 8-slot NI-compact DAQ compatible chassis. Modules used for these experiments included analog in, analog out, TTL command, digital out (relay), and thermocouple modules. The data acquisition and control tasks were run by a Virtual Instrument programmed in the NI LabVIEW graphical language in the RT Scan programming environment. This design allowed for a simple and deterministic control and data acquisition scheme.

Acquired measurement channels included thrust, chamber pressure, venturi pressures (inlet and throat differential) for oxidizer mass flow, and venturi temperature (necessary for determining GOX density in the venturi). Among the output channels were a TTL enable signal to activate the motor ignition system, analog out (0 - 5V) to modulate the maximum

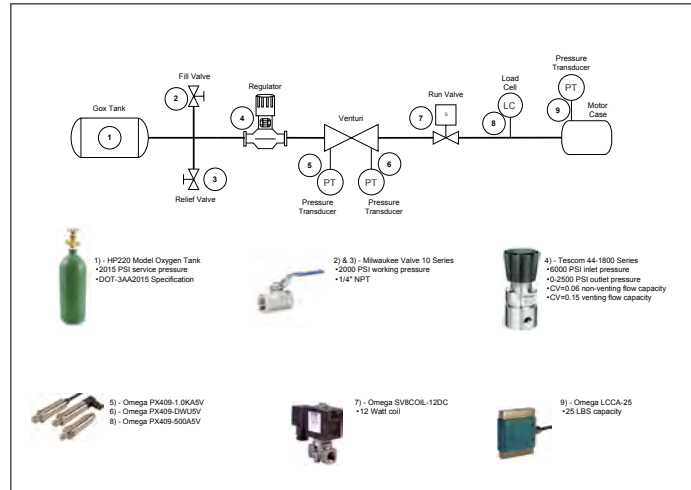


Fig. 4.1: KRMT Test Stand P&ID

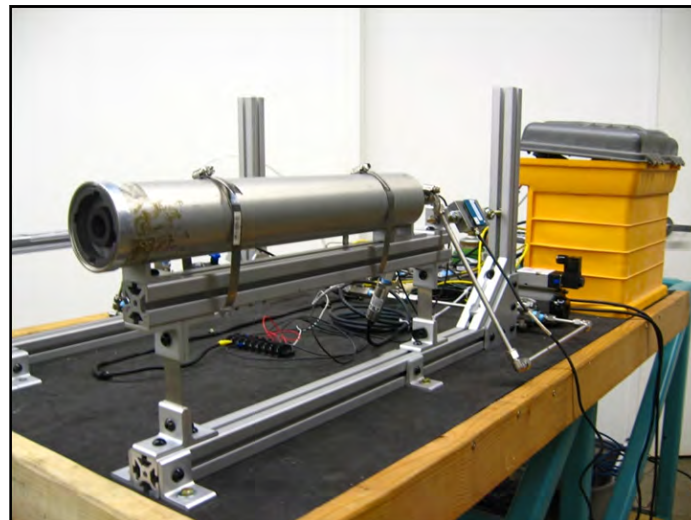


Fig. 4.2: Motor Installed on KRMT Test Stand

voltage delivered to the motor ignition system, and digital out to open the pneumatically-actuated GOX solenoid valve. The GOX supply was contained in a type-B gas cylinder, downstream of which was a variable-setting, pressure-reducing regulator. Downstream of the regulator was a custom venturi flow meter for mass flow rate measurement. Flow in the GOX line was controlled in a boolean fashion by a GOX-safe ball valve.

The regression tests were performed using a well-characterized motor that had been previously used for paraffin fuel regression tests. The motor was adapted from a commercially available 75-mm Cesaroni Pro75 motor case with a custom built injector cap, nozzle assembly, and insulation design. The system featured a novel non-pyrotechnic arc-ignition system developed at Utah State as a part of an earlier additive manufacturing campaign [35].

4.2 Fuel Grains and Assembly

The motor design takes advantage of FDM-processing to build the ignitor and fuel grain sections with “snap-together” interlocks that allow the grain segments to be manufactured separately and then assembled for combustion. The multiple grain segments were simultaneously manufactured on a Stratasys Dimension 1200es 3-D FDM printer using their standard density (0.975 g/cm^3) ABS stock material (See Figures 4.3 and 4.4). After soaking in the support material dissolving solution, the excess dissolving solution was removed from the bulk of the ABS material by evaporation in an evacuated chamber. The fuel sections were then assembled together using ABS cement on the “snap-together” fuel grain interlocks. Fig. 4.5 shows the grain interlock prototypes and an image of the assembled propellant grain with the embedded ignition electrodes. [35] Fig. 4.6 shows a schematic of the complete integrated motor system representing the “snap-together” fuel grain with the helical port structure. Fig. 4.7 shows the installed configuration firing in the Utah State University Propulsion Test Laboratory’s secure test cell.

Gaseous oxygen (GOX) was selected as the initial test oxidizer to allow the pressure-reducing regulator to be set to choke at a given mass flow, thus decoupling the oxidizer mass flow from the combustion chamber pressure, a key element to achieving accurate regression rate measurements at fixed oxidizer mass flow levels. For the purpose of this discussion, the



Fig. 4.3: Stratasys Dimension 1200es 3-D FDM Printer

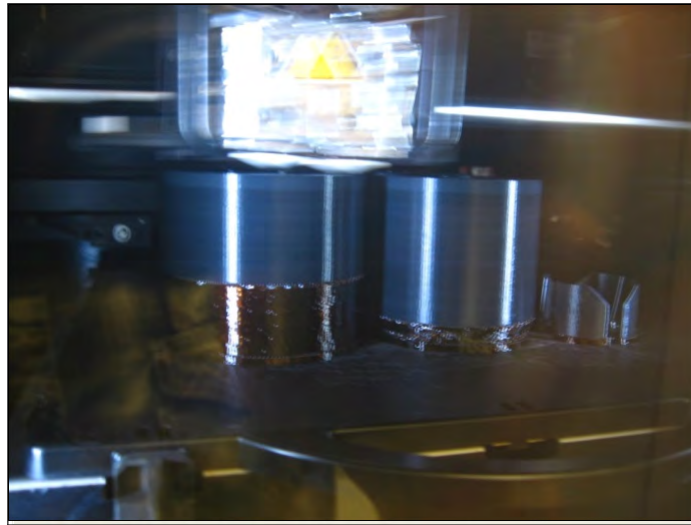


Fig. 4.4: Statasys Printer Simultaneously Building Multiple Fuel Grain Segments

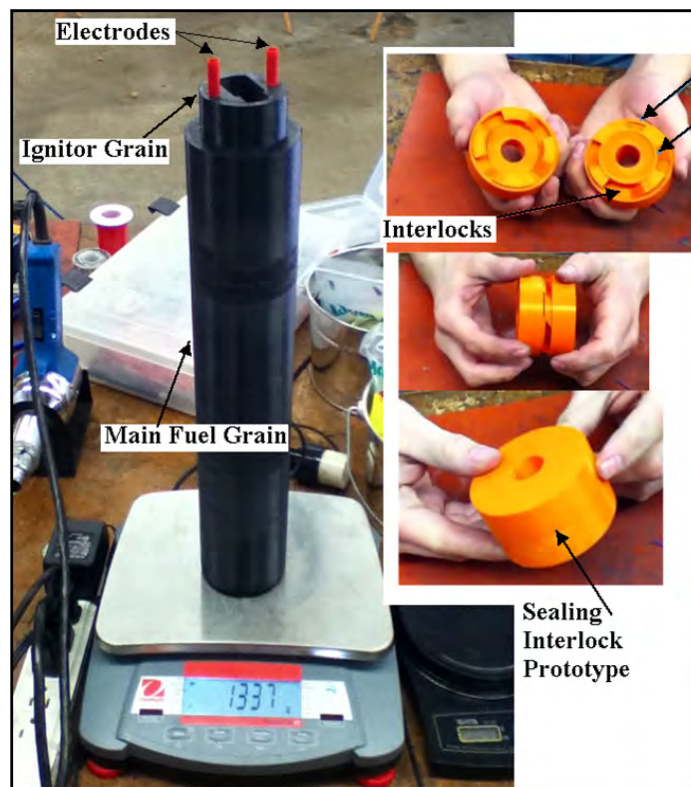


Fig. 4.5: Assembled 3d-printed Fuel Grain with Interlocking Segments

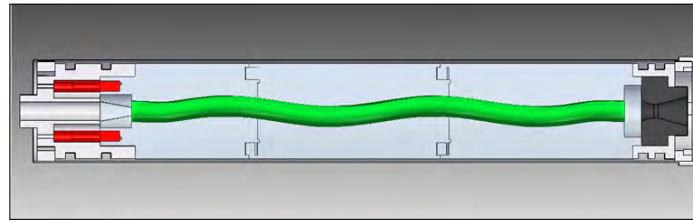


Fig. 4.6: Schematic of Lab Scale Hybrid Motor with Snap Together Helical Fuel Grains

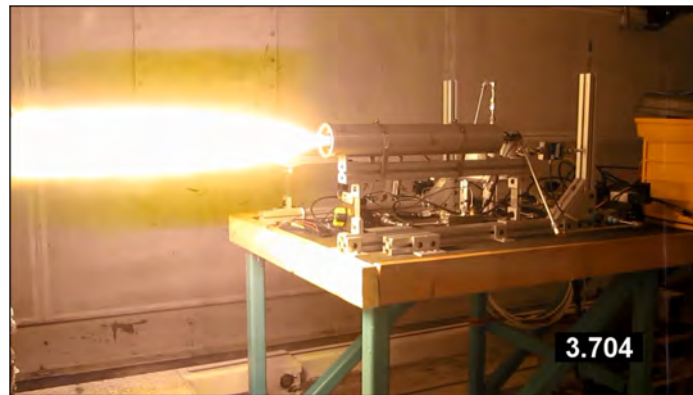


Fig. 4.7: Assembled 75-mm Motor Firing in Test Cell

Table 4.1: Tested Fuel Port Parameters

Grain No.	Fuel Grain Length, cm(L)	Initial Port Diameter, cm(D_o)	Initial Helix Diameter, cm(d)	Pitch, cm(P)	No. of Burns	Helix Ratio, (d/D_o)
1	35.98	2.026	-	-	3	-
2	35.98	1.524	0.762	15.24	5	.5
3	35.98	1.524	1.143	15.24	5	.75
4	35.98	1.524	1.524	15.24	6	1.0
5	22.86	1.524	0.762	15.24	5	.5
6	22.86	1.524	1.143	2.7	6	.75

ratio of the helix radius to the instantaneous port radius is referred to as the helix ratio. In total, six fuel grain configurations were tested with varying helix ratios (see Table 4.1). All helical fuel grains were manufactured with 10% of the fuel grain length dedicated to spiral the helical port back towards the center on both ends of the grain. The geometry of Grain No. 1 is a traditional straight port fuel grain, made to set baseline regression rate values. Fuel Grains 2-4 were all manufactured with the same 6" (15.24cm) helix pitch, but with varying Helix diameters to vary the helix ratio over a range of .5 to 1.0. Grain No. 5 was manufactured after the testing of grains 1-4, using the same helix parameters as Grain No. 2, but shorter in overall length to achieve an optimal O/F ratio. Finally, grain No. 6 was manufactured at this same short length, but with a much shorter pitch length (1.063 in or 2.7 cm). This was done to compare with the thrust level of Grain No. 1, since both fuel grains initially start with the same port run length.

4.3 Results

Fig. 4.8 presents cross-sectional images of the fuel grains at the conclusion of the testing campaign. For most of the fuel grains, it seems as though the original helical structure has been preserved. However, the cross section of Grain 6 has become nearly cylindrical. To analyze the effectiveness of these helical structures, the fuel regression rates were measured on each grain. Traditionally, this measurement is done by calculating an average rate over the length of the burn. For a straight-port fuel grain, this method is acceptable, however with the rapidly changing fuel port geometry of a helical fuel grain, a more rigorous method is required.

4.3.1 Measured Regression Rate

The instantaneous mean longitudinal fuel regression rate was calculated from the fuel massflow starting with

$$\bar{r} = \frac{\dot{m}_{fuel}}{\rho_{fuel} \cdot 2\pi \cdot \bar{r} \cdot L} \quad (4.1)$$



Fig. 4.8: Post-Test Fuel Grain Cross Sections

Rearranging Eq. 4.1 and integrating from the initial condition to the current time solves for the mean instantaneous fuel port diameter

$$\bar{r}(t) = \sqrt{r_0^2 + \int_0^t \frac{\dot{m}_{fuel}}{\rho_{fuel} \cdot \pi \cdot L} dt} \quad (4.2)$$

The effective port total massflux is estimated as

$$\bar{G}_{total} = \frac{\dot{m}_{ox} + \frac{5}{9} \cdot \dot{m}_{fuel}}{\pi \cdot r_0^2 + \int_0^t \frac{\dot{m}_{fuel}}{\rho_{fuel} \cdot \pi \cdot L} dt} \quad (4.3)$$

In Eq. 4.3 the “5/9ths” scaling rule presented previously is assumed to calculate the total effective fuel port massflux.

Fig. 4.9 compares the measured regression rates to the model predictions as a function of the total mass flux. The oxidizer massflux plotted on the horizontal axis and the regression rate plotted on the vertical. The plotted symbols represent the regression rate data derived from the test burns. The plotted lines represent the predicted regression rate calculated using Eqs. 2.27 and 3.5. The labels on each of the plotted lines correspond to the fuel port geometries of Table 4.1. Clearly, the helix pitch ratio affects the regression rate significantly. Initially, the helical port data exhibits a large amplification factor; but as the port burns, the

port cross section becomes more and more cylindrical and the helical effects on skin friction diminish with time. The modified model predictions agree quite well with the measured rates, with only the short pitch data showing any statistically significant deviations.

4.3.2 Amplification Factors

Fig. 4.10 presents the calculated model amplification factors as a function of the total oxidizer mass flux. For each of the helical geometries (grains 2-6), the skin friction, blowing suppression, and total amplification factors are plotted. Based on the model predictions, the skin friction increase is the dominating factor in the overall skin friction amplification, with the blowing suppression contributing to about 25% of the overall regression rate enhancement. As expected, the short pitch helix shows the highest initial regression rate increase, but also shows the greatest regression rate drop off as the fuel port opens up. Fig. 4.11 plots the calculated O/F ratios for each of the 6 fuel ports from table 4.1. As expected, the helical grains exhibit significantly lower O/F ratios when compared to the straight port grain due to the longer port run length.

4.3.3 Effect of Rotational Reynolds Number

It is also informative to plot the regression rate against the Reynolds number of the helical flow component calculated by

$$R_{e\omega} = \frac{\rho}{\mu} \cdot (\omega \cdot R_{helix}) \cdot S = \frac{G_{ox}}{\mu} \cdot \left(2\pi \cdot \frac{L}{P} \cdot R_{helix} \right) \quad (4.4)$$

since this parameter provides an idea of the measure of the centrifugal and skin friction effects of the helical flow field. Fig. 4.12 presents the results of this calculation where the rotational Reynolds number is plotted on the horizontal axis and the regression rate is plotted on the vertical. Curve fits of the data are also plotted showing the extrapolation down to essentially zero rotational Reynolds number. All curves for the helical fuel grains asymptotically approach the baseline regression value extrapolated from the data of Fig. 4.9 at low oxidizer mass flux. This result clearly indicates that the rotational flow velocity

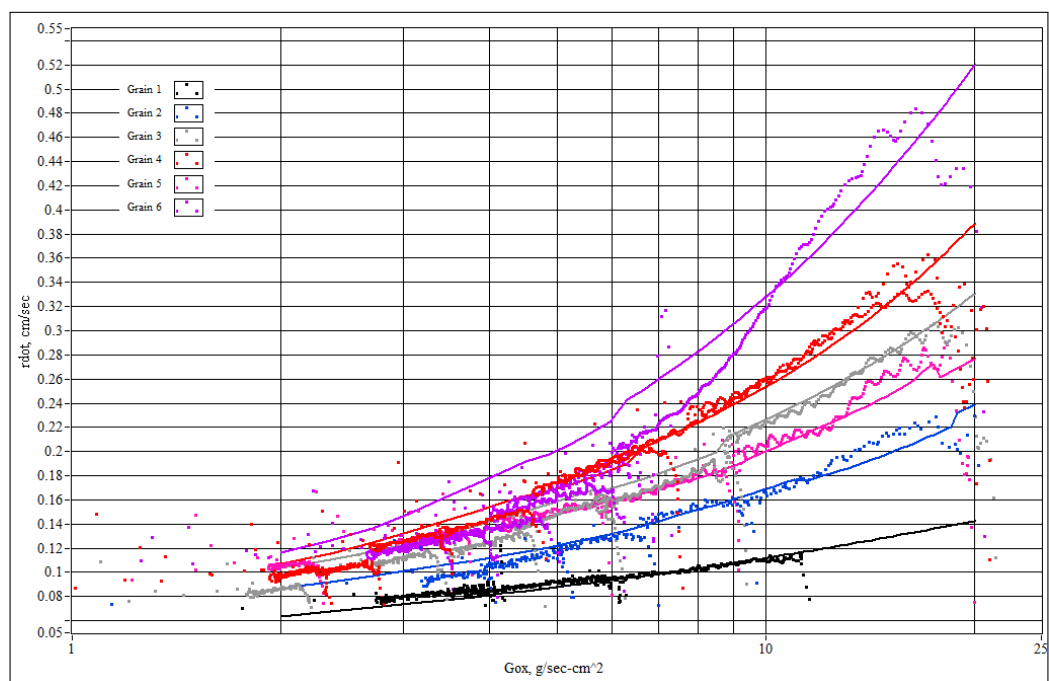


Fig. 4.9: GOX-ABS Regression Rate Data and Model Comparison for Straight-Bore and Helical Grains

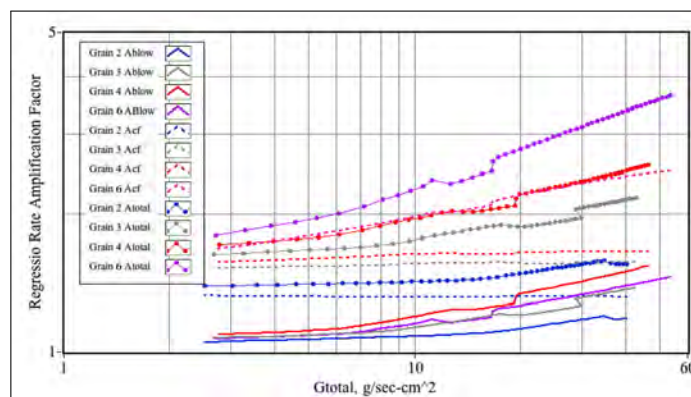


Fig. 4.10: Predicted Regression Rate Amplification Factors for Helical Fuel Ports

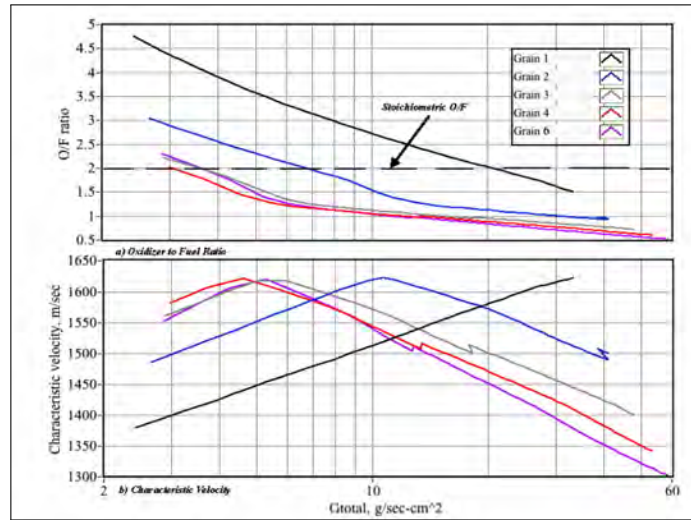


Fig. 4.11: Predicted O/F Ratios and Characteristic Velocity for Helical Fuel Ports

in the fuel port is a primary driver for the regression rate amplification. Any fuel structures that impart a significant rotational component to the flow will also significantly enhance the regression rate.

4.3.4 Volumetric Efficiency

Traditional straight fuel ports are fabricated with very long length-to-diameter ratios to increase the total burning area to increase thrust. These high aspect ratios can result in reduced fuel regression rate, poor volumetric efficiency, and a potential for lateral structural loading issues during high thrust burns. To demonstrate how helical fuel ports would improve this “volumetric efficiency,” Grain No. 6 was designed to have an initial fuel port length equal to that of the longer straight port of Grain No. 1. This design was chosen to show the large effect the helical fuel port would have on the chamber pressure of the motor because both grains would have the same initial oxidizer mass flux and burning area. Due to convenience, the same fuel grain length on Grain No. 5 (9 in or 22.86 cm) was used in this comparison to compare it to the longer 14 in (35.56 cm) Grain No. 1 since it has already been developed for testing. The results of this comparison test can be seen in Fig. 4.13 and Fig. 4.14

Fig. 4.13 shows the chamber pressure time histories of both Grain No. 1 and 6 over

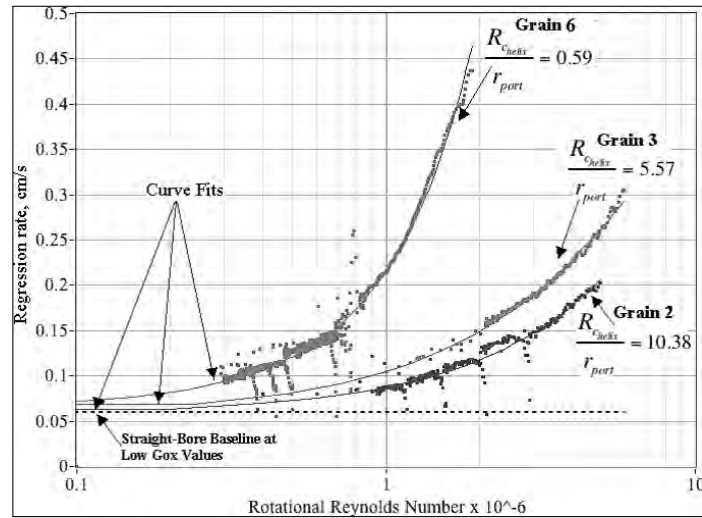


Fig. 4.12: Effect of Rotational Reynolds Number on Fuel Regression Rate

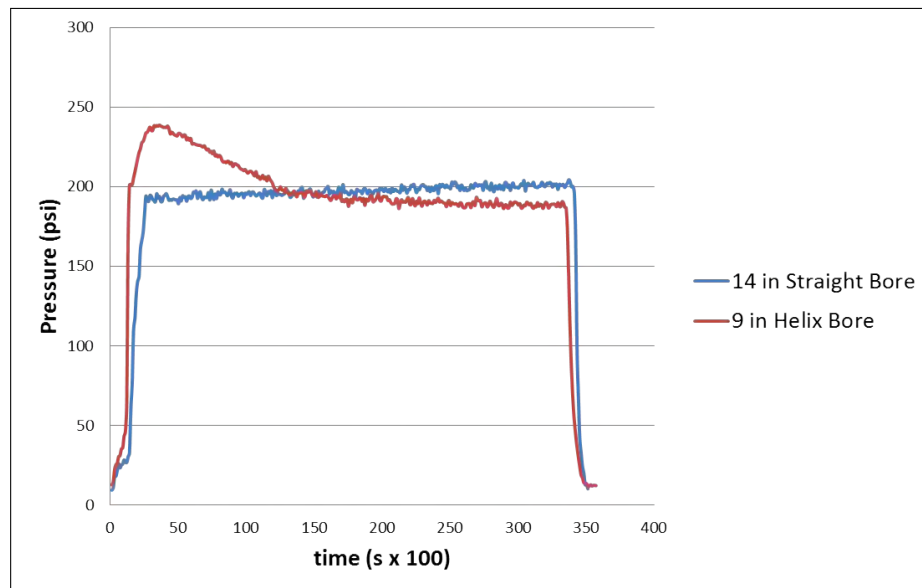


Fig. 4.13: Long vs. Short Grain Thrust Curve Comparison

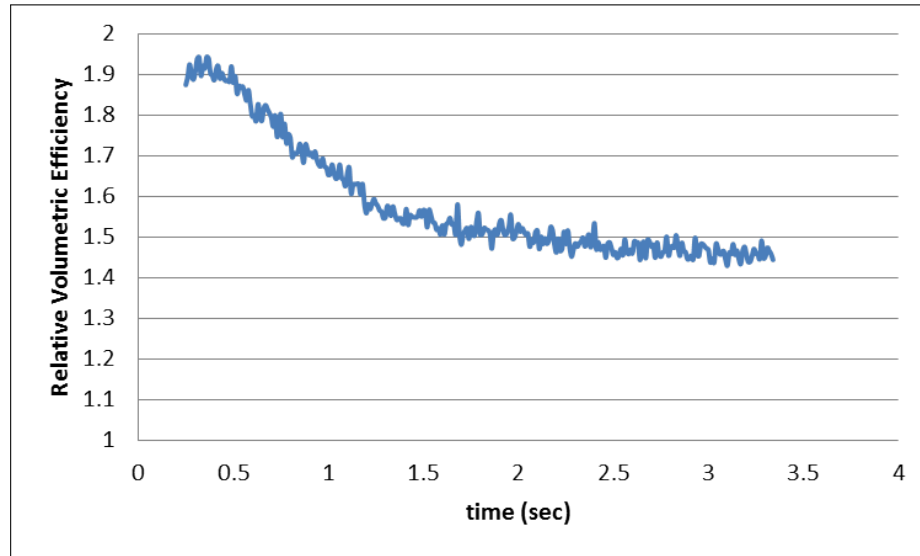


Fig. 4.14: Long vs. Short Grain Length Efficiency Comparison

the first few seconds of burn. It can be seen that for the first second of burn, the shorter helical motor has a higher chamber pressure than the longer straight port. After this point, the chamber pressure of the shorter motor diminishes below that of the longer straight port. However, to compare the “volumetric” efficiency of the two, the lengths of the motors were taken into consideration to make a dimensionless “motor length efficiency” term η . See Eq. 4.5.

$$\eta = \frac{P_{short} / L_{short}}{P_{long} / L_{long}} \quad (4.5)$$

P_{short} and L_{short} are the chamber pressure and overall grain length of the shorter helical grain, and P_{long} and L_{long} are the chamber pressure and overall grain length of the longer straight port grain. The term η represents the increased length efficiency of the short grain with respect to the longer (see Fig. 4.14). It’s worth noting again that the two tests were carried out using the same oxidizer mass flow rate and nozzle size. This analysis is not a central part of this thesis, but shows the potential of reducing the overall length of hybrid rocket fuel grains while maintaining high thrust levels. This test produced a length efficiency as high as 1.9, which with a dedicated study could be further optimized for various applications.

4.3.5 Optimal O/F Shift

O/F shifts in hybrid rocket motors are often expected due to the change of the exposed burn area and the change of the oxidizer mass flux throughout the burn. Most often, a traditional cylindrical fuel grain will have a burn exponent of greater than 0.5, meaning the O/F shifts from a more fuel-rich mixture to a more oxidizer-rich mix. An optimal propulsion system goal would be to maintain a burn exponent closest to 0.5 as possible to maintain performance at an optimal characteristic velocity (C^*). These helical fuel grain tests were not tested to optimize the burn exponents with respect to the helix ratio; however, the data received bracketed the upper and lower bounds of an optimal configuration that would maintain a near-optimal O/F ratio throughout the burn. As seen in Fig. 4.15, the fuel grains all have an O/F shift, with Grain No. 6 having the greatest shift and Grains No. 2 and 5 with the least.

After performing the initial tests of Grains 1-4, Grain No. 2 was seen to have a minimal O/F shift over the entirety of its burn, however with an average O/F of a less than optimal 0.9 (See Fig. 4.15). To achieve a more optimal C^* , for which the optimal O/F ratio for GOX/ABS is 1.5, a fuel grain with the same helical parameters as Grain 2 would have to be made in a shorter fuel grain. Using the simulations derived in previous sections, a new motor (Grain No. 5) was sized to achieve a more optimal O/F (see O/F curve for Grain No. 5 in Fig. OtoFMassflux). This redesign aimed to reduce the amount of burning surface area to increase the O/F to 1.5. The observed regression rate, however, was higher than expected (see Grain 5 in Fig. 4.9). It was found that one of the Marxman coefficients discussed in the Hybrid Regression Rate Theory Chapter ($L^{-0.2}$) wasn't taken into consideration and the regression rate was higher than expected, resulting in an O/F of around 1.2.

Though unexpected, the helix ratio of .5 flattens the O/F shift, with a burn exponent of nearly 0.5. Current research done at Utah State, in partnership with the NASA Armstrong Research Center, is being done to develop a throttle hybrid rocket motor using this helix ratio of .5 (See Fig. 4.16 and 4.17). The O/F on this motor has a large shift due to its deep throttle capability, however the .5 helix ratio maintains the O/F at an optimal level during

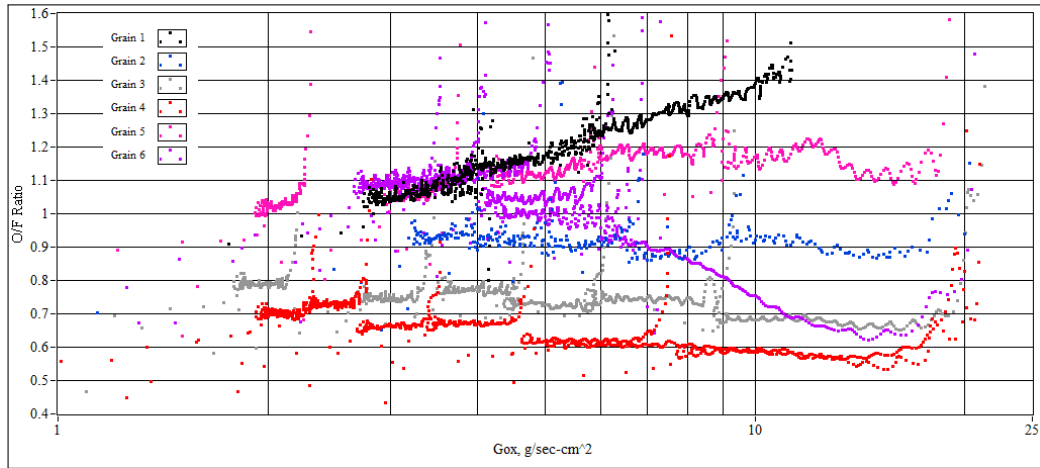


Fig. 4.15: O/F Ratios vs Oxidizer Massflux

the full-throttle portion of the burn.

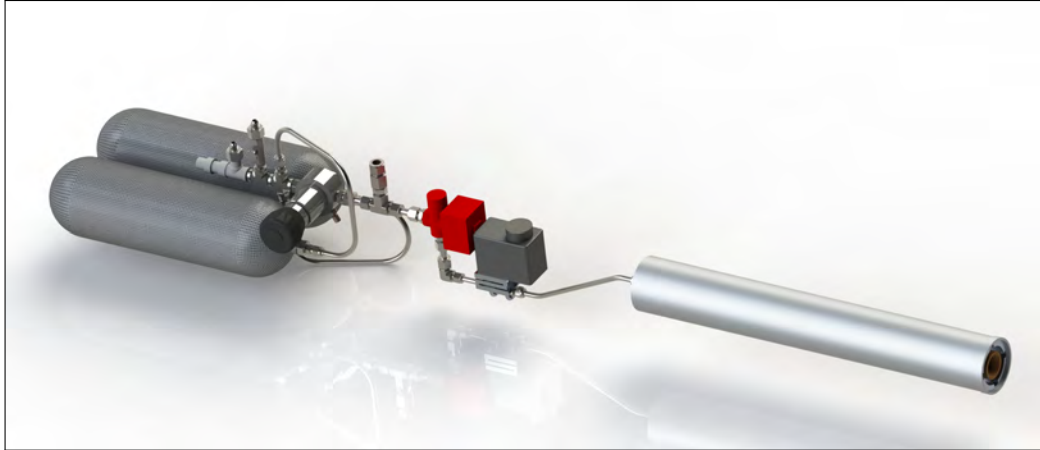


Fig. 4.16: NASA Armstrong Throttled Hybrid Rocket Motor

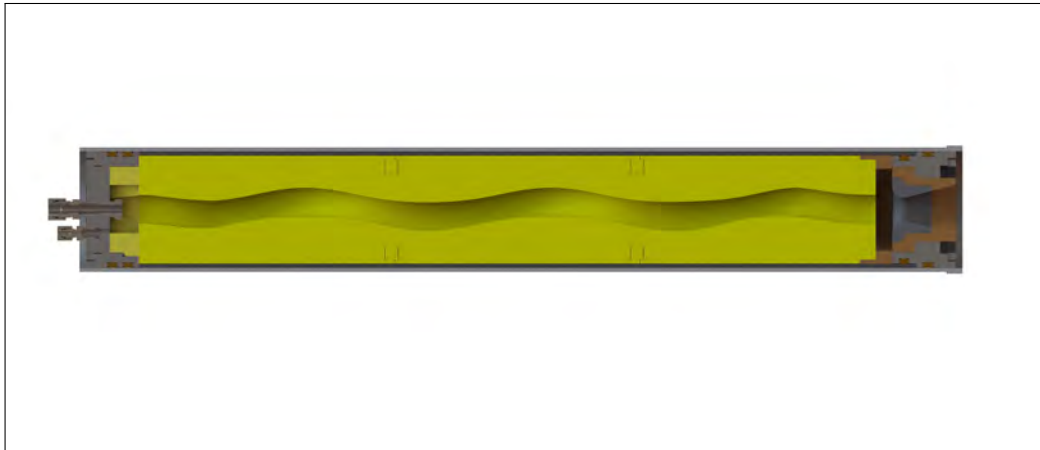


Fig. 4.17: Cross-Section of Throttled Hybrid Motor Case

Chapter 5

Conclusion

Hybrid rockets produce fuel regression rates typically 25% lower than solid propellant motors in the same thrust class. These lowered regression rates produce unacceptably high oxidizer-to-fuel (O/F) ratios and can result in motor instability, nozzle erosion, and reduced motor duty cycles. Several methods including multiple fuel ports, liquefying fuel materials, and grain metallization have been previously developed to increase regression rates; but each method has significant developmental issues.

This paper presents a new approach that uses first-principle fluid mechanics to enhance the fuel regression rate. This paper presents results from a development campaign that uses additive manufacturing to fabricate hybrid rocket fuel grains with embedded helical fuel port structures. These simple fuel structures have demonstrated a significant increase fuel regression rates – by a factor greater than 3 in some instances. The helical fuel port also increases the volumetric efficiency of the fuel grain by lengthening the internal flow path. The effectiveness of the helical structures was demonstrated using gaseous oxygen as oxidizer and acrylonitrile butadiene styrene (ABS) as the fuel component. Presented analysis has demonstrated that the rotational flow velocity within the fuel port is a primary driver for the regression rate amplification. Centrifugal flow patterns introduced by the embedded fuel port structures dramatically increase fuel regression rates by enhancing surface skin friction and reduce the effect of radial boundary layer “blowing” outflow. These two mechanisms work together to enhance the convective heat transfer to the fuel surface.

As the fuel grain burns and the helix ratio, defined as the ratio between the instantaneous fuel port radius and the helix loop radius, becomes small, the burn pattern becomes more and more like a cylindrical fuel grain. This produces a cylindrical final fuel grain pattern and reduces the potential for excessive un-burned fuel “slivers.” The slowed end-of-life

burn rate also reduces the potential for motor case burn-through. This type of behavior, however, was not sufficiently well-modeled due to a substantial reduction of burning area when the helical loops burned together during the tests. As a result, the model developed for helical fuel ports diverged from the experimental data, over-predicting the performance of the motor by the end of the motor’s burn. However, this helical model has a satisfactory fit for the rest of the fuel grains throughout the entirety of their respective burns. This model will work well for helical fuel ports that have a more “mild” pitch length with respect to the helix ratio. More work needs to be done to accurately model more “aggressive” helical fuel ports.

Because ABS fuel ports can be manufactured in an almost infinite variety of shapes using FDM processes, there exists the potential to “draw” high regression rate ABS fuel grains that mathematically optimize desired combustion properties including the ability to “hover” near the thermodynamically optimal point on the characteristic-velocity curve for a wide range of potential oxidizer mass flux levels. Fortunately, because the grains are built additively, if one can draw it, then one can build it.

5.0.6 Future Work

Helix Surface Area

Although the regression data fits well with the overlaid models (see Fig. 4.9), Grain No. 6’s regression model over-predicts the measured data throughout the burn. This type of behavior was expected due to the lack of understanding of how an “aggressive” helical fuel port’s surface burn area changes over the course of the burn. The surface area of the helix for the models shown on Fig. 4.9 was calculated as follows

$$A_{surf} = C_{port} \cdot L_{port} \quad (5.1)$$

C_{port} is the circumference of the fuel port, and L_{port} is the run length of the helix. As a helical fuel grain with a very high helix ratio (See Fig. 5.1) and short pitch burns, the

helical paths burn together, significantly reducing the exposed burning fuel surface area, resulting in a more cylindrical fuel port over the course of the burn (See Fig. 5.2). This loss of helical port surface area reduces the regression rate faster than the model can predict.

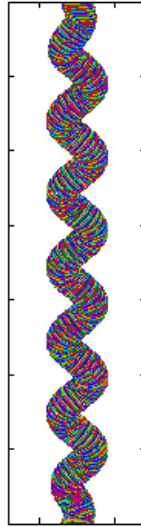


Fig. 5.1: Aggressive Helical Fuel Port Pre-Burn Visualization

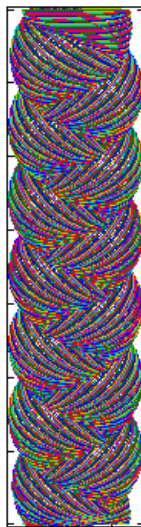


Fig. 5.2: Aggressive Helical Fuel Port Post-Burn Visualization

References

- [1] Anon, "Hazard Analysis of Commercial Space Transportation; Vol. 1: Operations, Vol. 2: Hazards, Vol. 3: Risk Analysis," *U.S. Dept. of Transportation, PB93-199040, Accession No. 00620693*, May 1988.
- [2] Cheng, C. G., Farmer, R. C., and Jones, H. S. ANS McFarlane, J. S., "Numerical Simulation of the Internal Ballistics of a Hybrid Rocket," *AIAA Paper 94-0554, 30th AIAA/ASME/SAE/ASEE Joint Propulsion Conference and Exhibit, Indianapolis, IN*, July, 1994.
- [3] Karabeyoglu, M. A., Stevens, J., and Cantwell, B. J., "Investigation of Feed System Coupled Low Frequency Combustion Instabilities in Hybrid Rockets," *AIAA 2007-5366, 43rd AIAA/ASME/SAE/ASEE Joint Propulsion Conference and Exhibit, Cincinnati, OH*, 8 - 11 July 2007.
- [4] Sutton, G. P. and Biblarz, O., *Rocket Propulsion Elements*, Wiley, 2010.
- [5] Karabeyoglu, M. A., "Hybrid Rocket Propulsion for Future Space Launch," *Stanford University Aero Astro 50th Year Anniversary Presentation*, May 09, 2008.
- [6] Ebeling, R. W. J., "Non-Sustaining Hybrid Propellant Grain," October 17, 1972.
- [7] Knuth, W. H., Chiaverini, M. J., Sauer, J. A., and Gramer, D. J., "Solid-Fuel Regression Rate Behavior of Vortex Hybrid Rocket Engines," *The Journal of Propulsion and Power, Vol. 18, 2002, pp. 600609*, 2002.
- [8] Karabeyoglu, M. A., Altman, D., and Cantwell, B. J., "Combustion of Liquefying Hybrid Propellants: Part 1, General Theory," *Journal of Propulsion and Power, Vol. 18, No. 3*, March, 2002.
- [9] Nakagawa, I., Hikone, S., and Suzuki, T., "A Study on the Regression Rate of Paraffin-based Hybrid Rocket Fuels," *AIAA 2009-4935, 45th AIAA/ASME /SAE/ASEE Joint Propulsion Conference & Exhibit, Denver, CO*, 28 July-1 August 2009.
- [10] Karabeyoglu, M. A., Zilliac, G., Cantwell, B. J., Dezilwa, S., and P., C., "Scale-up Tests of High Regression Rate Paraffin-Based Hybrid Rocket Fuels," *Journal of Propulsion and Power, Vol., No. 5*, Nov.-Dec., 2004.
- [11] Galfetti, L., Merotto, L., Biocchi, F., Maggi, F., and L. De Luca, L. T., "Ballistic and Rheological Characterization of Paraffin-Based Fuels for Hybrid Rocket Propulsion," *47th AIAA/ASME/SAE/ASEE Joint Propulsion Conference and Exhibit, San Diego CA*, 31 July-3 August 2011.
- [12] Anon, "Weapons Systems and Platforms (WP) Focus Area. Environmentally Friendly Sustainable Binder System for Energetic Materials," *Strategic Environmental Research and Development Program (SERDP), Exploratory Development (SEED) BAA-13-0002*, 2014, This proposal responds specifically to FY2014 SEED Statement of Need, WPSEED-14-01.

- [13] Whitmore, S. A., Peterson, Z. W., and Eilers, S. D., "Comparing Hydroxyl Terminated Polybutadiene and Acrylonitrile Butadiene Styrene as Hybrid Rocket Fuels," *AIAA J. Propulsion and Power*, Vol. 29, No. 3, May/June 2013.
- [14] Feldman, J., "Plastics-Materials of the 21st Century," .
- [15] Cha, J. and Co-authors, *Engineering Plastics Handbook, Chapter 6. Acrylonitrile-Butadiene-Styrene (ABS) Resin*, McGraw-Hill, 2006.
- [16] Kawata, K., Chung, H. L., and Itabashi, M., "Dynamic mechanical Behavior of HTPB Dummy Composite Propellant," *J. Advanced Composite Materials*, Vol. 3, No. 3, 1994.
- [17] Blom, H., Yeh, R., Wojnarowski, R., and Ling, M., "Detection of Degradation of ABS Materials via DSC," *Journal of Thermal Analysis and Calorimetry*, Vol. 83, No. 1, January 2006.
- [18] Fuller, J., Ehrlich, D., Lu, P., Jansen, R., and Homan, J., "Advantages of Rapid Prototyping for Hybrid Rocket Motor Fuel Grain Fabrication," *47th AIAA/ASME/SAE/ASEE Joint Propulsion Conference and Exhibit*, August 2011.
- [19] Bath, A., *Performance Characterization of Complex Fuel Port Geometries for Hybrid Rocket Fuel Grains*, Master's thesis, College of Engineering and Applied Sciences, Utah State University, December 2012.
- [20] Arnold, D., Boyer, J. E., Kuo, K. K., Desain, J. D., Curtiss, T. J., and Fuller, J. K., "Test of Hybrid Rocket Fuel Grains with Swirl Patterns Fabricated Using Rapid Prototyping Technology," *AIAA 2013, 4141, 49th AIAA/ASME/SAE/ASEE Joint Propulsion Conference, San Jose, CA*, July 14 - 17, 2013.
- [21] Marxman, G. and M. Gilbert, "Turbulent boundary layer combustion in the hybrid rocket," *Symposium (International) on Combustion*, Vol. 9, No. 1, 1963.
- [22] Marxman, G. A., Wooldridge, C. E., and Muzzy, R. J., "Fundamentals of Hybrid Boundary Combustion," *Progress in Astronautics and Aeronautics*, Vol. 15, No. 1, 1964.
- [23] Geankoplis, C., *Transport processes and separation process principles, 4th edition*, 2003.
- [24] White, F. M., *Viscous Fluid Flow*, McGraw-Hill, 1991.
- [25] McCabe, W. L., Smith, J., C., and Harriot, P., *Unit Operations of Chemical Engineering, 7th ed.*, McGraw-Hill, 2004.
- [26] Lees, L., "Convective Heat Transfer with Mass Addition and Chemical Reactions," *Combustion and Propulsion, 3rd AGARD Colloquium, New York, Pergamon Press*, 1958.
- [27] Eilers, S. D. and Whitmore, S. A., "Correlation of Hybrid Rocket Propellant Regression Measurements with Enthalpy-Balance Model Predictions," *AIAA J. Spacecraft and Rockets*, Vol. 45, No. 4, September/August, 2008.

- [28] Schlichting, H., *Boundary Layer Theory, Chapter 16*, McGraw-Hill, 1979.
- [29] Cantwell, B. J., "Similarity solution of fuel mass transfer, port massflux coupling in hybrid propulsion," *Journal of Engineering Mathematics (ISSN 0022 0833) Vol. 84, No. 1*, 2014.
- [30] Eilers, S. D. and Whitmore, S. A., "Correlation of Hybrid Rocket Propellant Regression Measurements with Enthalpy-Balance Model Predictions," *AIAA J. Spacecraft and Rockets, Vol. 45, No. 4*, September/August, 2008.
- [31] Whitmore, S. A., D., W. S., and P., M. D., "High Regression Rate Hybrid Rocket Fuel Grains with Helical Port Structures," *AIAA-2014-3751, 50th AIAA/ASME/SAE/ASEE Joint Propulsion Conference and Exhibit, Cleveland OH, 28-30 July 2014*.
- [32] White, C. M., "Friction factor and its relation to heat transfer, Transactions of the Institution of Chemical Engineers," *Trans. of Inst. of Chem. Eng., Vol. 18, No. 1.*, 1932.
- [33] Ito, H., "Friction Factor for Turbulent Flow in Curved Tube," *J. Basic Engineering, Vol. 81, No. 1.*, 1959.
- [34] Gnielinski, G. V., "Heat Transfer and Pressure Drop in Helically Coiled Tubes," *8th International Heat Transfer Conference, San Francisco, USA, Vol. 6, No. 1.*, 1986.
- [35] Whitmore, S. A., Inkley, N. R., and Merkley, D. P., "Development of a Power Efficient, Restart-Capable Arc Ignitor for Hybrid Rockets," *AIAA-2014-1943-765, 50th AIAA/ASME/SAE/ASEE Joint Propulsion Conference and Exhibit, Cleveland, OH, 28-30 July 2014*.